

COMET: Clustering Observables Modelled by Emulated perturbation Theory

Alexander Eggemeier,^{1*}† Benjamin Camacho-Quevedo,^{2,3} Andrea Pezzotta,⁴ Martin Crocce,^{2,3} Román Scoccimarro,⁵ Ariel G. Sánchez^{4,6}

¹Argelander Institut für Astronomie der Universität Bonn, Auf dem Hügel 71, 53121 Bonn, Germany

²Institute of Space Sciences (ICE, CSIC), Campus UAB, Carrer de Can Magrans, s/n, 08193 Barcelona, Spain

³Institut d'Estudis Espacials de Catalunya (IEEC), 08034 Barcelona, Spain

⁴Max-Planck-Institut für extraterrestrische Physik, Postfach 1312, Giessenbachstr., 85748 Garching, Germany

⁵Center for Cosmology and Particle Physics, Department of Physics, New York University, NY 10003, New York, USA

⁶Universitäts-Sternwarte München, Fakultät für Physik, Ludwig-Maximilians-Universität München, Scheinerstrasse 1, 81679 München, Germany

Accepted XXX. Received YYY; in original form ZZZ

ABSTRACT

In this paper we present COMET, a Gaussian process emulator of the galaxy power spectrum multipoles in redshift-space. The model predictions are based on one-loop perturbation theory and we consider two alternative descriptions of redshift-space distortions: one that performs a full expansion of the real- to redshift-space mapping, as in recent effective field theory models, and another that preserves the non-perturbative impact of small-scale velocities by means of an effective damping function. The outputs of COMET can be obtained at arbitrary redshifts, for arbitrary fiducial background cosmologies, and for a large parameter space that covers the shape parameters ω_c , ω_b , and n_s , as well as the evolution parameters h , A_s , Ω_K , w_0 , and w_a . This flexibility does not impair COMET's accuracy, since we exploit an exact degeneracy between the evolution parameters that allows us to train the emulator on a significantly reduced parameter space. While the predictions are sped up by two orders of magnitude, validation tests reveal an accuracy of 0.1 % for the monopole and quadrupole (0.3 % for the hexadecapole), or alternatively, better than 0.25σ for all three multipoles in comparison to statistical uncertainties expected for the *Euclid* survey with a tenfold increase in volume. We show that these differences translate into shifts in mean posterior values that are at most of the same size, meaning that COMET can be used with the same confidence as the exact underlying models. COMET is a publicly available Python package that also provides the tree-level bispectrum multipoles and Gaussian covariance matrices.

Key words: methods: data analysis; (cosmology:) cosmological parameters; (cosmology:) large-scale structure of Universe

1 INTRODUCTION

Models of galaxy clustering statistics inspired by perturbation theory will be one of the main avenues for extracting cosmological information from ongoing and upcoming galaxy surveys, such as the Dark Energy Spectroscopic Instrument (DESI; Levi et al. 2013) and *Euclid* (Laureijs et al. 2011). That is because on sufficiently large scales, where the validity of the perturbative models can be guaranteed, they reach an unparalleled degree of accuracy, making them a very robust and reliable analysis tool. However, even though perturbative methods have been frequently and successfully used in the analysis of past data sets (e.g. Sánchez et al. 2017; Beutler et al. 2017; Ivanov et al. 2020; d'Amico et al. 2020; Semenaite et al. 2022), they cannot be blindly applied to future measurements. The density field associated to each observed population of galaxies will be differently biased with respect to the underlying dark matter field, will have undergone different levels of non-linear evolution, and will be subject to different statistical uncertainties, all of which influence the range of scales

on which we can trust the perturbative models. Consequently, each new analysis will need to be accompanied by careful studies of their validity by propagating choices in the modelling, as well as the impact of potential systematics, onto the final results: the cosmological parameters.

Such a task requires running a large number of Monte Carlo Markov Chains (MCMC) in order to determine the posterior parameter distributions, each of which typically takes of the order $\mathcal{O}(10^6)$ likelihood evaluations for convergence. Although a single evaluation of the perturbation theory models is comparatively fast, even when performing full-shape fits, and can be executed in ~ 1 s (e.g. Chudaykin et al. 2020; Chen et al. 2021), this still amounts to considerable computational costs. We intend to greatly facilitate this task by constructing an emulator for various clustering statistics in perturbation theory, in particular the multipoles of the redshift-space galaxy power spectrum, that is capable of drastically reducing the time needed for making model predictions (see DeRose et al. 2022; Donald-McCann et al. 2023, for a similar approach). We thus follow a recent string of works, which introduced emulators as a means of overcoming the much higher computational costs of running simulations, which are needed to extend models of galaxy clustering into

* E-mail: aeggemeier@astro.uni-bonn.de

† Argelander Fellow

the deeply non-linear regime. This enabled efficient modelling of the non-linear matter power spectrum for a set of cosmological parameters (Heitmann et al. 2009; Euclid Collaboration et al. 2019; Giblin et al. 2019; Euclid Collaboration et al. 2021; Angulo et al. 2021), but in combination with a halo occupation distribution model also of the galaxy power spectrum (Kwan et al. 2015; Kobayashi et al. 2020), and the galaxy correlation function in redshift space (Zhai et al. 2019; Yuan et al. 2022). Furthermore, a hybrid approach that makes use of a perturbative expansion of the galaxy bias relation, but obtains all ingredients from simulations was proposed for the galaxy power spectrum in Zennaro et al. (2021); Aricò et al. (2022); Kokron et al. (2021); Pellejero Ibañez et al. (2022). While the accuracy of these emulators is limited by the usually small number of training samples, it is straightforward to build large training sets for models purely based on perturbation theory. Our demand is therefore somewhat different: we want a flexible emulator that covers a large space of model parameters, brings large improvements in computation time and yet does not compromise on the principal advantage of perturbation theory, its accuracy.

In order to satisfy that demand it is important to keep the parameter space over which the emulator is build as small as possible. As in Donald-McCann et al. (2023); Aricò et al. (2022), we make use of the fact that all model parameters related to the galaxy bias expansion can be factorised and so their dependency does not need to be emulated. However, what sets our emulator apart from these other works is that it is build around the recently proposed *evolution mapping* approach (Sánchez et al. 2022), which further limits the emulation parameter space. In this approach, the cosmological parameters are split into two classes: shape parameters, such as the physical baryon and cold dark matter densities, ω_b , ω_c , and the spectral index n_s , and evolution parameters, such as the Hubble parameter $h \equiv H_0/(100 \text{ km s}^{-1} \text{ Mpc}^{-1})$, the scalar amplitude of fluctuations A_s , the dark energy equation of state parameters, w_0 , w_a , and the curvature density parameter Ω_K . At any given redshift the evolution parameters can only affect the amplitude of the linear matter power spectrum, provided it is expressed in units of Mpc (opposed to the conventional $h^{-1} \text{ Mpc}$), and thus follow an exact degeneracy (Sánchez 2020; Sánchez et al. 2022). Evolution mapping exploits that degeneracy by mapping models with different evolution parameters from one to the other by simply relabelling the redshifts that correspond to the same value of σ_{12} , the RMS of density fluctuations in spheres of radius 12 Mpc. We show that this degeneracy extends to the models of perturbation theory considered here, although in redshift-space we additionally need to account for the dependence on the growth rate f . Hence, by training our emulator in terms of σ_{12} and f in combination with the shape parameters, we can model the effect of the full set of evolution parameters and at arbitrary redshifts. In redshift-space clustering we also need to account for the Alcock-Paczynski (AP) effect (Alcock & Paczynski 1979; Ballinger et al. 1996a), which requires the assumption of a fiducial background cosmology. We do not include the AP effect in the emulator itself, but in a separate step, and therefore retain more flexibility, which allows us to support any fiducial cosmologies.

This paper is organised as follows: in Sec. 2 we start by reviewing the perturbative expressions for the galaxy power spectrum multipoles, which our emulator is based on. In particular, we consider two separate models, which differ in their treatment of the real- to redshift-space mapping and show how they can be related. Readers familiar with this material can skip ahead to Sec. 3, where we describe in detail the evolution mapping approach, as well as further design choices and the computational performance of our emulator. In Sec. 4 we conduct a series of stringent validation tests of our

emulator and propagate any emulation uncertainties onto the posterior distributions of the model parameters, demonstrating no relevant loss in accuracy. We conclude in Sec. 5 with a comparison to related works and an overview of the capabilities of our Python package COMET.

2 OVERVIEW OF PERTURBATION THEORY MODELS

In this work, we consider the emulation of the redshift-space power spectrum multipoles of biased tracers for two different perturbative models. These models differ solely in their treatment of redshift-space distortions with one performing a full expansion of the real-to-redshift space mapping, while the other partly retains the non-perturbative nature of this mapping. Examples of the first category of models are the recent effective field theory (EFT) models of Ivanov et al. (2020) and d’Amico et al. (2020), which introduce a series of counterterms that are meant to capture the effect from small-scale, virialised velocities of galaxies on the power spectrum. Models, such as TNS (Taruya et al. 2010) or the one proposed by Sánchez et al. (2017), fall into the second category and account for the virialised velocity impact via an effective damping function that represents the velocity difference generating function (VDG). For the remainder of this paper we will refer to these two models as EFT and VDG models, respectively.

As an overview, the galaxy power spectrum in the EFT model is generally decomposed into four different terms,

$$P_{gg,\text{EFT}}(\mathbf{k}) = P_{gg,\text{SPT}}^{\text{tree}}(\mathbf{k}) + P_{gg,\text{SPT}}^{1\text{-loop}}(\mathbf{k}) + P_{gg}^{\text{stoch}}(\mathbf{k}) + P_{gg}^{\text{ctr}}(\mathbf{k}), \quad (1)$$

where the first two refer to the leading and next-to-leading (tree-level and one-loop, respectively) contributions from standard perturbation theory (SPT), which result from an expansion of the real to redshift-space mapping, the non-linear evolution of the matter and velocity fields, and galaxy bias (see Sec. 2.1 and 2.2). The third term accounts for stochastic effects due to the impact from highly non-linear scales on the galaxy bias relation, while the last term represents the series of counterterms (see Sec. 2.3) that are meant to absorb any sensitivities of the one-loop term to modes beyond the reach of perturbation theory and, as stated before, the effect from virialised velocities. The above expression is furthermore supplemented by a procedure (infrared resummation) that takes into account the damping of baryon acoustic oscillations (BAO) from large-scale relative displacements, the details of which will be presented in Sec. 2.4. The galaxy power spectrum in the VDG model involves all the same ingredients, and we show that it can be related to the EFT model as follows:

$$P_{gg,\text{VDG}}(\mathbf{k}) = W_\infty(\mathbf{k}) [P_{gg,\text{EFT}}(\mathbf{k}) - \Delta P(\mathbf{k})], \quad (2)$$

where W_∞ denotes the effective damping function and $\Delta P(\mathbf{k})$ is a correction term that stems from the fact that not the full real to redshift-space mapping is expanded perturbatively and will be computed in Sec. 2.1.

Throughout this section and for the remainder of this paper we assume the plane-parallel approximation for redshift-space distortions¹ and work under the Fourier transform convention

$$\delta(\mathbf{x}) = \int_{\mathbf{k}} e^{-i\mathbf{k}\cdot\mathbf{x}} \delta(\mathbf{k}). \quad (3)$$

All \mathbf{k} -space integrals are written using the short-hand notation

¹ This means that all pairs of galaxies have the same line-of-sight, which we take to be the \hat{z} -direction.

$\int_{\mathbf{k}_1, \dots, \mathbf{k}_n} \equiv \int d^3k_1 / (2\pi)^3 \cdots d^3k_n / (2\pi)^3$, and in configuration space we analogously use $\int_{\mathbf{x}_1, \dots, \mathbf{x}_n} \equiv \int d^3x_1 \cdots d^3x_n$.

2.1 Redshift-space power spectra in EFT and VDG models

The mapping from real-space position \mathbf{x} to redshift-space position \mathbf{s} in the plane-parallel approximation is given by:

$$\mathbf{s} = \mathbf{x} - f u_z(\mathbf{x}) \hat{z}, \quad (4)$$

where u_z is the line-of-sight peculiar velocity normalised such that $\theta = \nabla \cdot \mathbf{u} = \delta$ in linear theory (i.e. $\mathbf{v} \equiv -f\mathcal{H}\mathbf{u}$), f is the growth rate and \mathcal{H} the conformal Hubble rate. This yields for the galaxy density perturbations in redshift-space (Scoccimarro et al. 1999),

$$\delta_s(\mathbf{k}, z) = \int_{\mathbf{x}} e^{i\mathbf{k} \cdot \mathbf{x}} e^{-ifk_z u_z(\mathbf{x})} D_s(\mathbf{x}) \quad (5)$$

where we assumed that the Jacobian of the map in Eq. (4) can be approximated $J = |1 - f\nabla_z u_z| \simeq 1 - f\nabla_z u_z$ and $D_s(\mathbf{x}) \equiv \delta_g(\mathbf{x}) + f\nabla_z u_z(\mathbf{x})$ is a combination of the galaxy density contrast δ_g and the gradient of u_z along the line-of-sight. Expanding δ and \mathbf{u} in perturbation theory, yields the perturbation theory kernels in redshift-space Z_n (Scoccimarro et al. 1999)

$$\delta_s(\mathbf{k}, z) = \sum_{n=1} D^n(z) \int_{\mathbf{k}_1, \dots, \mathbf{k}_n} \delta_D(\mathbf{k} - \mathbf{k}_{1\dots n}) Z_n(\mathbf{k}_1, \dots, \mathbf{k}_n) \times \delta_L(\mathbf{k}_1) \cdots \delta_L(\mathbf{k}_n), \quad (6)$$

which not only contain information about the redshift-space distortions, but also about galaxy bias, which we describe next in Sec. 2.2 (see Appendix A for explicit expressions). This leads to the standard perturbation theory expressions for the power spectrum in redshift-space at leading and next-to-leading (one-loop) order,

$$P_{gg, \text{SPT}}^{\text{tree}}(\mathbf{k}) = Z_1(\mathbf{k})^2 P_L(k) \quad (7)$$

$$P_{gg, \text{SPT}}^{1\text{-loop}}(\mathbf{k}) = 2 \int_{\mathbf{q}} [Z_2(\mathbf{k} - \mathbf{q}, \mathbf{q})]^2 P_L(|\mathbf{k} - \mathbf{q}|) P_L(q) + 6 P_L(k) \int_{\mathbf{q}} Z_3(\mathbf{k}, \mathbf{q}, -\mathbf{q}) P_L(q) \quad (8)$$

where \mathbf{k} is described by its magnitude k and its cosine μ with respect to the fixed line-of-sight in the plane-parallel approximation, $\mu \equiv \hat{\mathbf{k}} \cdot \hat{z}$, and P_L is the linear power spectrum in which we have absorbed the redshift dependence.

In order to relate the power spectrum in the VDG model to the SPT computation we start from the exact expression of the redshift-space galaxy power spectrum that can be derived from the redshift-space map in Eq. (4), written in terms of the pairwise velocity generating function $\mathcal{M}(\lambda, \mathbf{r})$ (see Scoccimarro 2004, for a derivation):

$$P_{gg}(\mathbf{k}) = \int_{\mathbf{r}} e^{i\mathbf{k} \cdot \mathbf{r}} \left\{ [1 + \xi_{gg}(r)] \mathcal{M}(\lambda, \mathbf{r}) - 1 \right\}, \quad (9)$$

where $\xi_{gg}(r)$ is the real-space galaxy two-point correlation function at separation r and $\lambda \equiv -ifk\mu$. As shown in Scoccimarro (2004); Taruya et al. (2010), the pairwise velocity generating function can be decomposed into the following building blocks of connected correlators:

$$[1 + \xi_{gg}(r)] \mathcal{M}(\lambda, \mathbf{r}) = W(\lambda, \mathbf{r}) \left[\left\langle e^{\lambda \Delta u_z} D_s(\mathbf{x}) D_s(\mathbf{x}') \right\rangle_c + \left\langle e^{\lambda \Delta u_z} D_s(\mathbf{x}) \right\rangle_c \left\langle e^{\lambda \Delta u_z} D_s(\mathbf{x}') \right\rangle_c \right], \quad (10)$$

where Δu_z is the difference in line-of-sight peculiar velocities at

positions \mathbf{x} and $\mathbf{x}' = \mathbf{x} + \mathbf{r}$. The prefactor $W(\lambda, \mathbf{r}) \equiv \exp \left\langle e^{\lambda \Delta u_z} \right\rangle_c$ is the velocity difference generating function. The velocity difference at separation r is most sensitive to small-scale modes, since large-scale modes with $kr \lesssim 1$ contribute the same velocity to both \mathbf{x} and \mathbf{x}' . Therefore the VDG model attempts to keep this term non-perturbative and instead replaces it by an effective damping function, calculated in the large-scale limit ($r \rightarrow \infty$), given by (Sánchez et al. 2017)

$$W_\infty(\lambda) = \frac{1}{\sqrt{1 - \lambda^2 a_{\text{vir}}^2}} \exp \left(\frac{\lambda^2 \sigma_v^2}{1 - \lambda^2 a_{\text{vir}}^2} \right), \quad (11)$$

where a_{vir} is a free parameter that contributes to small-scale velocity dispersion and controls the kurtosis of the VDG, i.e. the limit $a_{\text{vir}} = 0$ corresponds to Gaussian velocity differences. The fact that $a_{\text{vir}} \neq 0$ reflects the well-known result that even in the large-scale limit the probability distribution function of pairwise velocities is non-Gaussian with significant exponential tails (Sheth 1996; Juszkiewicz et al. 1998; Scoccimarro 2004; Cuesta-Lazaro et al. 2020).

In the VDG model, the remaining terms in square brackets in Eq. (10) are treated perturbatively, i.e. expanding the exponentials to give an expression consistent to one-loop order. As in the EFT model this expansion includes galaxy bias and stochastic terms, as well as counterterms from small-scale modes, while all resulting expressions are evaluated using BAO-damped linear power spectra as described in Section 2.4. Since Eqs. (9-10) are of course compatible with perturbation theory, the relation between the EFT and VDG power spectra is found by computing only the additional terms $\Delta P(\mathbf{k})$ that result from the expansion of the velocity difference generating function. Up to one-loop order it is sufficient to expand the exponential as $\exp \left\langle e^{\lambda \Delta u_z} \right\rangle_c \approx 1 + \lambda^2 / 2 \left\langle \Delta u_z^2 \right\rangle$, which leads to one extra term given by

$$\Delta P(k, \mu) = \int_{\mathbf{r}} e^{i\mathbf{k} \cdot \mathbf{r}} \left[\frac{\lambda^2}{2} \left\langle \Delta u_z^2 \right\rangle \left\langle D_s(\mathbf{x}) D_s(\mathbf{x}') \right\rangle \right] = \lambda^2 \sigma_v^2 P_{D_s D_s}(k, \mu) - \lambda^2 \int_{\mathbf{q}} \frac{q_z^2}{q^4} P_{\theta\theta}(q) P_{D_s D_s}(\mathbf{k} - \mathbf{q}), \quad (12)$$

where $P_{D_s D_s}$ and $P_{\theta\theta}$ are the power spectra of the $D_s(\mathbf{x})$ field and the velocity divergence, both of which are evaluated at leading order in Eq. (12), which implies $P_{D_s D_s}(\mathbf{k}) = P_{gg, \text{SPT}}^{\text{tree}}(\mathbf{k})$. The linear velocity dispersion, σ_v , appearing in the first term on the second line of Eq. (12) is given by:

$$\sigma_v^2 = \frac{1}{3} \int_{\mathbf{k}} \frac{P_{\theta\theta}(k)}{k^2} = \frac{1}{3} \int_{\mathbf{k}} \frac{P_L(k)}{k^2}. \quad (13)$$

Finally, since W_∞ does not depend on scale \mathbf{r} , we can pull it out of the integral in Eq. (9), from which Eq. (2) follows.

We note that the VDG model as presented here differs from the TNS model (Taruya et al. 2010) in the effective damping function W_∞ and in that the square bracket in Eq. (10) includes all contributions from quadratic bias, both local and nonlocal (Sánchez et al. 2017).

2.2 Galaxy bias expansion and stochasticity

In perturbation theory we predict the clustering of biased tracers, such as dark matter halos or galaxies, by first relating their over-densities to a series of properties of the underlying dark matter field. This is known as the galaxy bias expansion (see Desjacques et al. (2018a) for a comprehensive review), where each property (in the following also denoted as *operator*) captures an effect of the large-scale environment on the formation and evolution of galaxies, and the strength

of that effect is encoded in the associated galaxy bias parameters. While the values of the bias parameters cannot be computed from first principles and also depend on the selection of the observed population of tracers, the various operators to be taken into account at each order of perturbation theory can be derived based on symmetry considerations (McDonald & Roy 2009; Chan et al. 2012; Assassi et al. 2014; Senatore 2015; Mirbabayi et al. 2015; Desjacques et al. 2018a; Eggemeier et al. 2019).

Choosing the set of operators proposed in Eggemeier et al. (2019), and showing only quantities that are relevant for the computation of the power spectrum at next-to-leading order, results in the following expansion:

$$\delta_g = b_1 \delta + \frac{b_2}{2} \delta^2 + \gamma_2 \mathcal{G}_2(\Phi_v) + \gamma_{21} \mathcal{G}_{21}(\varphi_2, \varphi_1) + b_{\nabla^2} \nabla^2 \delta + \epsilon_g + \dots, \quad (14)$$

with each term being evaluated at position \mathbf{x} and redshift z . The two Galileon operators \mathcal{G}_2 and \mathcal{G}_{21} , which quantify the impact of large-scale tides at second and third order, are defined as (sums over repeated indices are implied)

$$\mathcal{G}_2(\Phi_v) \equiv \nabla_i \nabla_j \Phi_v \nabla_i \nabla_j \Phi_v - \left(\nabla^2 \Phi_v \right)^2, \quad (15)$$

$$\mathcal{G}_{21}(\varphi_2, \varphi_1) \equiv \nabla_i \nabla_j \varphi_2 \nabla_i \nabla_j \varphi_1 - \nabla^2 \varphi_2 \nabla^2 \varphi_1, \quad (16)$$

where $\Phi_v = \nabla^{-2} \theta$ is the velocity potential and φ_i are the potentials of Lagrangian perturbation theory, satisfying:

$$\nabla^2 \varphi_1 = -\delta, \quad \nabla^2 \varphi_2 = -\mathcal{G}_2(\varphi_1). \quad (17)$$

Transformed into Fourier space, these relations give rise to the galaxy bias kernel functions given in Eqs. (A9) and (A10).

There are a number of other, equivalent galaxy bias bases in the literature with a different choice of operators, and their corresponding bias parameters can be mapped into those described above via simple linear transformations. For instance, the basis used by Assassi et al. (2014); Ivanov et al. (2020) contains two different operators and their bias parameters are related to the ones here as

$$\gamma_2 = b_{\mathcal{G}_2}, \quad \gamma_{21} = -\frac{4}{7} (b_{\mathcal{G}_2} + b_{\Gamma_3}), \quad (18)$$

whereas the four bias parameters defined in d'Amico et al. (2020) (denoted here with a tilde) convert into ours as follows:

$$b_1 = \tilde{b}_1, \quad b_2 = 2 (-\tilde{b}_1 + \tilde{b}_2 + \tilde{b}_4), \quad \gamma_2 = -\frac{2}{7} (\tilde{b}_1 - \tilde{b}_2), \quad (19)$$

$$\gamma_{21} = -\frac{2}{147} (11\tilde{b}_1 - 18\tilde{b}_2 + 7\tilde{b}_3).$$

While the default in COMET is the expansion based on Eq. (14), it is possible to specify bias parameters corresponding to either of the other two bases above.

The last two terms in Eq. (14) represent the relevant contributions from higher-derivative operators and stochasticity, respectively. The former arise when taking into account that gravitational collapse occurs within patches of finite size R , meaning that on distance scales of comparable magnitude, the galaxy over-density at position \mathbf{x} can no longer be assumed to depend on the matter properties at the *same* position alone. Expanding this spatial non-locality perturbatively leads to terms scaling as $\sim R^2 \nabla^2 \mathcal{O}$ with $\mathcal{O} = \{\delta, \delta^2, \mathcal{G}_2, \dots\}$ (Desjacques 2008; McDonald & Roy 2009; Desjacques et al. 2010, 2018a) and assuming that the scale R is of similar order as the non-linearity scale of the matter field, the term $\nabla^2 \delta$ is the only one relevant for the power spectrum at next-to-leading order. Its bias parameter does not appear in the kernels in Eqs. (A9) and (A10), because in Sec. 2.3 we will

absorb it into the definition of one of the counterterms that carries the same scale dependence.

Finally, the stochastic field ϵ_g is meant to summarise all highly non-linear effects on galaxy formation that are not captured by the perturbative expansion. The corresponding wavemodes are uncorrelated with those accessible in perturbation theory and thus all of the large-scale fields appearing in Eq. (14), meaning that on large scales their contribution appears stochastic (Dekel & Lahav 1999; Taruya & Soda 1999; Matsubara 1999). They therefore enter the galaxy power spectrum as an independent term, the stochastic power spectrum $\langle \epsilon_g(\mathbf{k}_1) \epsilon_g(\mathbf{k}_2) \rangle = (2\pi)^3 P_{\epsilon_g} \epsilon_g(k_1) \delta_D(\mathbf{k}_{12})$, which can be expanded in the low- k regime as (Desjacques et al. 2018a; Eggemeier et al. 2021):

$$P_{\epsilon_g} \epsilon_g(k) = \frac{1}{\bar{n}} \left(N_0^P + N_{2,0}^P k^2 + \dots \right), \quad (20)$$

where \bar{n} denotes the mean number density of the tracer population and we have defined the two stochastic bias parameters, N_0^P and $N_{2,0}^P$. Through the redshift-space mapping the galaxy power spectrum is also sensitive to a stochastic component in the gradient of the line-of-sight velocity field, $\epsilon_{\nabla_z u_z}$, which leads to one additional term (Perko et al. 2016; Desjacques et al. 2018b) that was shown to account for the small-scale velocity dispersion (Desjacques et al. 2018b). We parametrise this term as follows:

$$P_{\epsilon_g \epsilon_{\nabla_z u_z}}(k, \mu) = \frac{N_{2,2}^P}{\bar{n}} \mathcal{L}_2(\mu) k^2 + \dots, \quad (21)$$

where $\mathcal{L}_2(\mu)$ denotes the second Legendre polynomial², such that the total stochastic contribution to the galaxy power spectrum is given by

$$P_{gg}^{\text{stoch}}(k, \mu) = P_{\epsilon_g} \epsilon_g(k) + P_{\epsilon_g \epsilon_{\nabla_z u_z}}(k, \mu). \quad (22)$$

Since in the VDG model the impact from small-scale velocities is encoded in the effective damping function W_∞ and not expanded perturbatively, it is likely that the second term in Eq. (22) is of subordinate importance in that case.

2.3 Definition of counterterms

The loop integrals in Eq. (8) or Eq. (12) are performed over the entire range of scales, even those where perturbation can no longer be applied. In order to construct a consistent theory, one needs to introduce a series of *counterterms* with adjustable amplitudes (i.e., a free parameter per counterterm), which are able to absorb any sensitivity to non-linear modes that might arise in the large-scale limit. It was shown e.g. in Senatore & Zaldarriaga (2014); Desjacques et al. (2018b) that the required leading counterterms for the galaxy power spectrum in redshift-space scale as $\sim \mu^{2n} k^2 P_L(k)$ with $n = 0, 1, 2$, assuming them for simplicity to be local in time. The first of these scales exactly like the higher-derivative bias contribution $\nabla^2 \delta$ (see Sec. 2.2) and so we can absorb its coefficient, $b_{\nabla^2 \delta}$, into the corresponding counterterm parameter. The same counterterm also absorbs the leading effect from a breakdown of the perfect fluid approximation for the matter field (Pueblas & Scoccimarro 2009; Baumann et al. 2012; Carrasco et al. 2012). Moreover, Desjacques et al. (2018b) demonstrated that the other two counterterms with

² Using the Legendre polynomial in the definition of $N_{2,2}^P$ is an arbitrary choice, which simply guarantees that this term can only contribute to the quadrupole of the power spectrum in the absence of Alcock-Paczynski distortions.

$n = 1$ and $n = 2$ can account for the relevant velocity bias effects, which we have neglected in our description so far.

In total, we therefore introduce another three free parameters, c_0 , c_2 and c_4 , and define the contribution from the leading order counterterms to the galaxy power spectrum as follows:

$$P_{gg}^{\text{ctr,LO}}(k, \mu) = -2 \sum_{n=0}^2 c_{2n} \mathcal{L}_{2n}(\mu) k^2 P_L(k), \quad (23)$$

where instead of the scaling with μ^{2n} we used Legendre polynomials of order $2n$. This simply corresponds to a linear transformation of the counterterm parameters, and means that each of them predominantly contributes to only a single power spectrum multipole.

The perturbative expansion of the velocity difference generating function in case of the EFT model can also be regarded as a higher-derivative expansion, scaling roughly as $\sim (\mu k \sigma_v)^{2n} P_{gg, \text{SPT}}^{\text{tree}}(\mathbf{k})$, with Eq. (12) representing the term relevant at the one-loop level ($n = 1$). However, the length scale associated with this expansion is σ_v^{-1} , which could potentially be significantly different from the non-linearity scale of the matter field. In particular, if σ_v^{-1} is smaller than the non-linearity scale, this would imply that terms relevant at higher than one-loop should be retained in that expansion as well. For that reason, [Ivanov et al. \(2020\)](#) include the next-order term in the model for the galaxy power spectrum with a free amplitude that is meant to marginalise over such potential contributions:

$$P_{gg}^{\text{ctr,NLO}}(k, \mu) = c_{\text{nlo}} (\mu k f)^4 P_{gg, \text{SPT}}^{\text{tree}}(\mathbf{k}), \quad (24)$$

so that the full counterterm power spectrum reads:

$$P_{gg}^{\text{ctr}}(k, \mu) = P_{gg}^{\text{ctr,LO}}(k, \mu) + P_{gg}^{\text{ctr,NLO}}(k, \mu). \quad (25)$$

Since the NLO term is purely coming from the expansion of the velocity difference generating function, we do not include it in case of the VDG model.

2.4 Infrared resummation

The model presented in the previous sections provides a good description of the broadband of the anisotropic galaxy power spectrum on mildly non-linear scales, but exhibits a non negligible difference in terms of the amplitude of the BAO wiggles (e.g. [Baldauf et al. 2015](#)). The latter are most sensitive to large-scale bulk flows, which are responsible for the smearing of the BAO signal via the large-scale relative displacement field.

Following a perturbative approach, corrections to the matter power spectrum can be resummed at each wavenode k by taking into account the effect of fluctuations on larger scales, i.e. at $q < k$. At leading order, the net effect on the matter power spectrum is that of a damping factor, which only acts on the BAO wiggles. From a practical point of view, it is standard practice to split the linear matter power spectrum into a smooth and wiggly component ([Baldauf et al. 2015](#); [Blas et al. 2016](#)), such that

$$P_L(k) = P_{\text{nw}}(k) + P_w(k). \quad (26)$$

The wiggle/no-wiggle split is carried out making use of the same implementation suggested in [Vlah et al. \(2016\)](#); [Osato et al. \(2019\)](#). This reads

$$P_{\text{nw}}(k) = P_{\text{EH}}(k) \mathcal{F} \left[\frac{P_L(k)}{P_{\text{EH}}(k)} \right], \quad (27)$$

and consists in a rescaling of the original formula for the featureless matter power spectrum $P_{\text{EH}}(k)$ first presented in [Eisenstein & Hu \(1998\)](#), and adjusted to match the broadband amplitude of the linear

matter power spectrum. We choose the band filter \mathcal{F} to be Gaussian, with its functional form defined by

$$\mathcal{F}[f(k)] = \frac{1}{\sqrt{(2\pi) \log_{10}(\lambda)}} \int d(\log_{10}(q)) f(q) \times \exp \left[-\frac{(\log_{10}(k) - \log_{10}(q))^2}{2 (\log_{10}(\lambda))^2} \right], \quad (28)$$

where $\log_{10}(\lambda / (h^{-1} \text{Mpc})) = 0.25$.

At leading order, the infrared-resummed matter power spectrum can then be written as the sum of the smooth component and the damped wiggly one, such that ([Baldauf et al. 2015](#); [Blas et al. 2016](#))

$$P_{\text{mm}}^{\text{IR-LO}}(k) = P_{\text{nw}}(k) + e^{-k^2 \Sigma^2} P_w(k), \quad (29)$$

where

$$\Sigma^2 = \frac{1}{6\pi^2} \int_0^{k_s} P_{\text{nw}}(q) \left[1 - j_0 \left(\frac{q}{k_{\text{osc}}} \right) + 2j_2 \left(\frac{q}{k_{\text{osc}}} \right) \right] dq \quad (30)$$

is the two point function of the relative displacement field evaluated at the BAO scale. Here, j_n is the n -th order spherical Bessel function, $k_{\text{osc}} = 1/\ell_{\text{osc}}$ is the wavenode corresponding to the reference BAO scale $\ell_{\text{osc}} = 110 h^{-1} \text{Mpc}$, and k_s is the ultraviolet integration limit. Even though in principle the resummation of modes should be carried out for all $q < k$, it has become standard practice to fix this upper limit to an intermediate scale. In our implementation we adopt³ $k_s = 0.14 \text{Mpc}^{-1}$.

At next-to-leading order, the IR-resummed matter power spectrum receives additional contributions, along with the standard one-loop corrections sourced by higher powers of the density field. The final expression then reads ([Baldauf et al. 2015](#); [Blas et al. 2016](#))

$$P_{\text{mm}}^{\text{IR-NLO}}(k) = P_{\text{nw}}(k) + \left(1 + k^2 \Sigma^2 \right) e^{-k^2 \Sigma^2} P_w(k) + P^{1\text{-loop}} \left[P_{\text{mm}}^{\text{IR-LO}} \right] (k), \quad (31)$$

where the square brackets in the second line of Eq. (31) indicate that the one-loop integrals are evaluated using the leading order IR-resummed power spectrum instead of the linear power spectrum.

When considering the redshift-space galaxy power spectrum, the most notable difference is that the damping factor now also carries a dependence on the line-of-sight, such that, at leading order, we can write ([Ivanov & Sibiryakov 2018](#))

$$P_{\text{gg}}^{\text{s,IR-LO}}(k, \mu) = \left(b_1 + f\mu^2 \right)^2 \left[P_{\text{nw}}(k) + e^{-k^2 \Sigma_{\text{tot}}^2(\mu)} P_w(k) \right]. \quad (32)$$

The angular dependence of the new damping factor can be expressed as

$$\Sigma_{\text{tot}}^2(\mu) = \left[1 + f\mu^2(2 + f) \right] \Sigma^2 + f^2 \mu^2 (\mu^2 - 1) d\Sigma^2, \quad (33)$$

where

$$d\Sigma^2 = \frac{1}{2\pi^2} \int_0^{k_s} P_{\text{nw}}(q) j_2 \left(\frac{q}{k_{\text{osc}}} \right) dq. \quad (34)$$

At next-to-leading order, we can then write ([Ivanov & Sibiryakov](#)

³ Note that the value for k_s is defined in units of Mpc^{-1} opposed to $h \text{Mpc}^{-1}$ since COMET internally works in Mpc units, see Sec. 3.

2018):

$$\begin{aligned}
P_{\text{gg}}^{s,\text{IR-NLO}}(k, \mu) = & \\
& \left(b_1 + f\mu^2 \right)^2 \left[P_{\text{nw}}(k) + \left(1 + k^2 \Sigma_{\text{tot}}^2(\mu) \right) e^{-k^2 \Sigma_{\text{tot}}^2(\mu)} P_{\text{w}}(k) \right] + \\
& + P_{\text{gg}}^{s,1\text{-loop}} [P_{\text{nw}}](k) + \\
& + e^{-k^2 \Sigma_{\text{tot}}^2(\mu)} \left(P_{\text{gg}}^{s,1\text{-loop}} [P_{\text{nw}} + P_{\text{w}}](k) - P_{\text{gg}}^{s,1\text{-loop}} [P_{\text{nw}}](k) \right), \tag{35}
\end{aligned}$$

where, once again, square brackets indicate that we are evaluating the one-loop terms by either plugging in the total linear matter power spectrum ($P_{\text{nw}} + P_{\text{w}}$) or just the smooth component (P_{nw}).

3 EMULATOR DESIGN

Our emulator is designed around a number of key ideas that minimise the emulation parameter space, while simultaneously keeping the emulator highly flexible, as well as applicable to arbitrary fiducial background cosmologies and a continuous range of redshifts. This is achieved by 1) employing the *evolution mapping* approach of Sánchez et al. (2022), 2) an exact treatment of Alcock-Paczynski distortions, and 3) a separate emulation of all contributions that are proportional to a unique combination of galaxy bias parameters. In the following we describe these ideas and further design choices in detail.

3.1 Evolution mapping

The evolution mapping approach classifies the dependence on cosmological parameters into two groups: shape parameters, Θ_{s} , which determine the shape of the linear power spectrum $P_L(k|z)$, and evolution parameters, Θ_{e} , which at any given redshift only affect its amplitude. Examples of the former include the physical densities of radiation, baryons, cold dark matter and neutrinos, as well as the scalar spectral index,

$$\Theta_{\text{s}} = (\omega_{\gamma}, \omega_b, \omega_c, \omega_{\nu}, n_s, \dots), \tag{36}$$

while the latter class contains the scalar amplitude of the primordial power spectrum, the curvature and dark energy density parameters, as well as any parameters that describe the time evolution of the dark energy equation of state,

$$\Theta_{\text{e}} = (A_s, \omega_K, \omega_{\text{DE}}, w_{\text{DE}}(z), \dots). \tag{37}$$

Crucially, it was shown in Sánchez (2020); Sánchez et al. (2022) that when the linear power spectrum is expressed in units of Mpc (opposed to the traditional h^{-1} Mpc), all evolution parameters follow an exact degeneracy. This means that their joint effect can be summarised by the value of a single parameter, with a convenient choice being σ_{12} , the RMS of matter fluctuations in spheres of radius $R = 12$ Mpc, as suggested by Sánchez et al. (2022). The evolution mapping relation can then be expressed as

$$P_L(k|z, \Theta_{\text{s}}, \Theta_{\text{e}}) = P_L(k|\Theta_{\text{s}}, \sigma_{12}(z, \Theta_{\text{s}}, \Theta_{\text{e}})), \tag{38}$$

which states that at fixed values of Θ_{s} different choices of Θ_{e} can be transformed into each other by relabelling the redshifts that correspond to the same value of σ_{12} .

We can extend this concept to the perturbation theory models for biased tracers in redshift space that were discussed in Sec. 2. These models can be split into individual terms $P_{\mathcal{B}}(\mathbf{k}|z)$ that are proportional to different combinations of galaxy bias parameters \mathcal{B} . Each of these terms is a functional of the linear power spectrum and

depends otherwise only on the growth rate of structures $f(z)$.⁴ For that reason and using Eq. (38) we can write

$$\begin{aligned}
P_{\mathcal{B}}(\mathbf{k}|z, \Theta_{\text{s}}, \Theta_{\text{e}}) = & P_{\mathcal{B}}\{ \mathbf{k} | f(z, \Theta_{\text{s}}, \Theta_{\text{e}}), \\
& P_L(q|\Theta_{\text{s}}, \sigma_{12}(z, \Theta_{\text{s}}, \Theta_{\text{e}})) \}, \tag{39}
\end{aligned}$$

implying that the cosmology and redshift dependence of the perturbation theory models can be fully captured in terms of the shape parameters, the growth rate and σ_{12} . We will exploit this observation to make our emulator applicable to an arbitrary number of evolution parameters and for a continuous range of redshifts, thus giving it a high degree of flexibility.

3.2 Application of Alcock-Paczynski distortions and VDG damping function

The analysis of galaxy clustering data sets requires the assumption of a fiducial background cosmology, which is used to convert the measured redshifts and angular positions of the galaxies into comoving distance scales. Any differences between the true and fiducial cosmological parameters lead in general to anisotropic distortions of the power spectrum, commonly denoted as Alcock-Paczynski (AP) distortions. They are described by two parameters that quantify the rescaling of the distance scales parallel and perpendicular to the line-of-sight and are given by the ratios of the Hubble parameter and the comoving transverse distance in the true and fiducial cosmologies at the mean redshift of the galaxy sample⁵:

$$q_{\parallel} \equiv \frac{H(z_m|\Theta_{\text{s, fid}}, \Theta_{\text{e, fid}})}{H(z_m|\Theta_{\text{s}}, \Theta_{\text{e}})} \tag{40}$$

$$q_{\perp} \equiv \frac{D_M(z_m|\Theta_{\text{s}}, \Theta_{\text{e}})}{D_M(z_m|\Theta_{\text{s, fid}}, \Theta_{\text{e, fid}})}. \tag{41}$$

They are determined by a combination of the shape and evolution parameters, such that following the approach of Sec. 3.1 it is not possible to include the AP effect implicitly (which is not desirable anyway, since that implies the emulator is built with a fixed choice of fiducial cosmology). Instead, we could include q_{\parallel} and q_{\perp} as additional parameters in the emulator, but this would increase the emulation parameter space with potentially negative impacts on the overall accuracy of the emulator. For that reason we opt for emulating $P_{\mathcal{B}}(\mathbf{k}|z)$ without AP distortions and fold in their effect analytically in a separate step.

Another reason for not including the AP factors in the emulator itself is that we can also separately apply the effective damping function W_{∞} in the VDG model (see Sec. 2.1). As W_{∞} may depend on model parameters Θ_{W} (in addition to Θ_{s} and Θ_{e}), such as a_{vir} , that do not factorise, we can thus further limit the total number of parameters whose dependence needs to be emulated. Therefore, given the emulated $P_{\mathcal{B}}(k', \mu'|z)$, we compute the final multipoles by performing the integration

$$\begin{aligned}
P_{\mathcal{B}, \ell}(k|z, \Theta_{\text{s}}, \Theta_{\text{e}}) = & \frac{2\ell + 1}{2q_{\perp}^2 q_{\parallel}} \int_{-1}^1 d\mu \mathcal{L}_{\ell}(\mu) P'_{\mathcal{B}}(k', \mu'|z, \Theta_{\text{s}}, \Theta_{\text{e}}) \\
& \times W_{\infty}(k', \mu'|z, \Theta_{\text{s}}, \Theta_{\text{e}}, \Theta_{\text{W}}), \tag{42}
\end{aligned}$$

⁴ The growth rate cannot be fully factorised because it also affects the damping term in the IR resummation procedure (see Sec. 2.4), in particular Eq. (33).

⁵ We note that depending on the chosen unit system (Mpc vs. h^{-1} Mpc), H and D_M need to be given either in units of $\text{km s}^{-1} \text{Mpc}^{-1}$ and Mpc, or $\text{km s}^{-1} (h^{-1} \text{Mpc})^{-1}$ and $h^{-1} \text{Mpc}$, respectively.

Table 1. Bias contributions to the power spectrum at linear and one-loop order, which scale as P_L and P_L^2 , respectively.

\mathcal{B}	b_1^2	b_1	1	b_1^2	$b_1 b_2$	$b_1 \gamma_2$	$b_1 \gamma_{21}$	b_2^2	$b_2 \gamma_2$	γ_2^2	b_2	γ_2	γ_{21}	c_0	c_2	c_4	$b_1^2 c_{\text{nlo}}$	$b_1 c_{\text{nlo}}$	c_{nlo}
linear	✓	✓	✓											✓	✓	✓	✓	✓	✓
one-loop		✓	✓	✓	✓	✓	✓	✓	✓	✓	✓	✓	✓						

where $W_\infty = 1$ in case of the EFT model and primes denote quantities in the fiducial cosmology. They are related to those in the true cosmology as follows (Ballinger et al. 1996b):

$$k' = \frac{k}{q_\perp} \left[1 + \mu^2 (F^{-2} - 1) \right]^{1/2} \quad (43)$$

$$\mu' = \frac{\mu}{F} \left[1 + \mu^2 (F^{-2} - 1) \right]^{-1/2}, \quad (44)$$

where $F \equiv q_\parallel/q_\perp$. We note that the dependence of W_∞ on the shape and evolution parameters enters through the growth rate and the velocity dispersion, which is a functional of the linear power spectrum (see Eq. 13). That means that as for $P_{\mathcal{B}}$ the cosmology and redshift dependence of the damping term can be fully captured by Θ_s , the growth rate and σ_{12} .

The expression in Eq. (42) assumes that the power spectrum multipoles are estimated in infinitesimally thin shells k and for a continuous range of μ values. Both of these assumptions are not satisfied for actual measurements, where the multipoles are computed from discrete grids in Fourier space and by averaging over all wave modes that fall into shells of given widths (see e.g. Scoccimarro 2015). As shown in Taruya et al. (2013) this leads to sizeable deviations from what Eq. (42) would predict, in particular for the higher-order multipoles and for k values close to the fundamental frequency, k_f , of the grid used for the measurements. As described in more detail in Appendix B, one can account for these discreteness effects in the theoretical predictions, which we have implemented as an option in COMET. Up to scales $k \sim 60 k_f$ this comes at no additional computational cost compared to the computation via Eq. (42).

3.3 Emulated quantities

As is clear from the previous two sections, the task of our emulator is to provide the contributions $P_{\mathcal{B}}(k|z)$. In total there are 17 different contributions to take into account, summarised in Table 1. For $\mathcal{B} = b_1$ and $\mathcal{B} = 1$ we combine linear and one-loop terms, while for $\mathcal{B} = b_1^2$ we emulate them separately, allowing our emulator to also provide the IR resummed linear power spectrum, which can be useful for other computations. The stochastic contributions (involving the noise parameters N_0^P , $N_{2,0}^P$ and $N_{2,2}^P$) do not appear in this list because they do not depend on any cosmological quantities themselves and since we apply AP distortions and the finger-of-god damping separately (see Eq. 42), we can include them exactly.

3.3.1 Projection into multipoles and reconstruction of anisotropic power spectrum

In order to avoid having to emulate the full two-dimensional dependence of $P_{\mathcal{B}}$ on k and μ , we project the angular dependence into multipoles,

$$P_{\mathcal{B},\ell}(k) = \frac{2\ell + 1}{2} \int_{-1}^1 d\mu \mathcal{L}_\ell(\mu) P_{\mathcal{B}}(k, \mu), \quad (45)$$

and emulate only the monopole, quadrupole and hexadecapole, from which we reconstruct the 2D power spectra using the Legendre ex-

pansion. This procedure would be exact if all of the contributions contain powers of, at most, μ^4 . However, the redshift-space galaxy power spectrum contains terms up to μ^8 and, moreover, the dependence of the IR damping factor on μ^2 leads to non-zero multipoles for all even ℓ . Our reconstruction using only information up to the hexadecapole therefore introduces an error that becomes more relevant for the higher-order multipoles computed through Eq. (42). In order to approximately correct for that we include the $\ell = 6$ multipole $P_{\mathcal{B},6}$, evaluated at fixed redshift $z = 1$ and for a fixed set of Λ CDM cosmological parameters taken from the *Planck* TT,TE,EE+lowE+lensing constraints (Planck Collaboration et al. 2020) in the Legendre expansion:

$$P_{\mathcal{B}}(k|z, \Theta_s, \Theta_e) \approx \sum_{\ell=0}^2 P_{\mathcal{B},2\ell}(k|z, \Theta_s, \Theta_e) \mathcal{L}_{2\ell}(\mu) + P_{\mathcal{B},6} \left\{ k|f(z, \Theta_s, \Theta_e), P_L(k|\Theta_s^{\text{Planck}}, \sigma_{12}(z, \Theta_s, \Theta_e)) \right\} \mathcal{L}_6(\mu). \quad (46)$$

Our notation highlights that the fixed Planck values only enter through the shape parameters affecting the linear power spectrum, while the dependence of the growth rate and σ_{12} on the shape and evolution parameters is correctly accounted for. This is achieved by splitting up each $P_{\mathcal{B},6}$ into contributions with different powers of f and scaling their amplitude as follows:

$$P_{\mathcal{B},6}|_{\text{Planck}} \rightarrow \left(\frac{\sigma_{12}(z, \Theta_s, \Theta_e)}{\sigma_{12}(z=1, \Theta_s^{\text{Planck}}, \Theta_e^{\text{Planck}})} \right)^{2L} P_{\mathcal{B},6}|_{\text{Planck}}, \quad (47)$$

where $L = 1$ for all terms indicated as linear in Table 1 and $L = 2$ for the one-loop terms.⁶ In Sec. 4.4 we quantify the inaccuracies introduced by Eq. (46) and demonstrate that they are negligible.

3.3.2 Constructing ratios with the linear power spectrum

The amplitude of $P_{\mathcal{B},\ell}$ can be subject to large variations over the full range of values that the emulated parameters can assume. As that makes the emulation more difficult, we instead emulate the ratios, $\beta_{\mathcal{B},\ell}$, of $P_{\mathcal{B},\ell}$ and the linear power spectrum (excluding IR resummation), which significantly reduces the dynamical range of the relevant quantities. After emulating the ratios we then need to multiply again by the linear power spectrum, for which we build a separate emulator. However, this emulator can be constructed over the shape parameters

⁶ In this way only the dependence of the IR damping term on f and σ_{12} is not correctly taken into account, but instead computed for $z = 1$ and at the fixed Planck cosmological parameters.

Table 2. Emulator parameter space and the supported range of values.

Parameter	Min. emulator range	Max. emulator range
ω_b	0.0205	0.02415
ω_c	0.085	0.155
n_s	0.92	1.01
σ_{12}	0.2	1.0
f	0.5	1.05

alone, as shown by the following (exact) computation:

$$\begin{aligned}
P_{\mathcal{B},\ell}(k|z, \Theta_s, \Theta_e) &= \beta_{\mathcal{B},\ell}(k|\Theta_s, \sigma_{12}, f) P_L(k|\Theta_s, \sigma_{12}) \\
&= \beta_{\mathcal{B},\ell}(k|\Theta_s, \sigma_{12}, f) P_L(k|z=1, \Theta_s, \Theta_e^{\text{fixed}}) \\
&\quad \times \left(\frac{\sigma_{12}}{\sigma_{12}(z=1, \Theta_s, \Theta_e^{\text{fixed}})} \right)^2, \quad (48)
\end{aligned}$$

where we set $\sigma_{12} = \sigma_{12}(z, \Theta_s, \Theta_e)$ and used that the dependence on σ_{12} can be factored out of the linear power spectrum by evaluating P_L at fixed redshift and evolution parameters and rescale the amplitude accordingly.⁷ The value of $\sigma_{12}(z=1, \Theta_s, \Theta_e^{\text{fixed}})$ can be obtained as an integral over $P_L(k|z=1, \Theta_s, \Theta_e^{\text{fixed}})$, but instead we find it is more efficient to include an emulator for the former as a function of only Θ_s . As noted in Sec. 3.2 the finger-of-god damping factor in the VDG model depends on the velocity dispersion and a computation similar to that in Eq. (48) shows that it is sufficient to predict the value of $\sigma_v(z=1, \Theta_s, \Theta_e^{\text{fixed}})$, which we also emulate as a function of the shape parameters.

3.3.3 Summary

In summary, we thus require an emulation of the following quantities:

- (i) $\beta_{\mathcal{B},\ell}(k|\Theta_s, \sigma_{12}, f)$ for $\ell = 0, 2, 4$ and each \mathcal{B} from Table 1 ,
- (ii) $P_L(k|z=1, \Theta_s, \Theta_e^{\text{fixed}})$,
- (iii) $\sigma_{12}(z=1, \Theta_s, \Theta_e^{\text{fixed}})$,
- (iv) $\sigma_v(z=1, \Theta_s, \Theta_e^{\text{fixed}})$.

We evaluate the ratios and P_L on a range of scales extending from $7 \times 10^{-4} \text{ Mpc}^{-1}$ to 0.35 Mpc^{-1} , using a total number of 106 points, chosen such that they provide a dense sampling on scales relevant for the BAO wiggles.

3.4 Parameter space and training process

3.4.1 Parameter ranges

Our emulator is constructed for a total of five parameters: in addition to f and σ_{12} , we consider the three shape parameters ω_b , ω_c , and n_s . Each of them is allowed to vary within the ranges given in Table 2, which for the latter three were chosen to span roughly a 12 , 30 and 11σ interval around the *Planck* 2018 best-fit values, respectively.

⁷ The fixed values for z and the evolution parameters are not essential, but we used $z=1$, $h=0.695$, $A_s=2.2078559$ and all other potential evolution parameters set to zero.

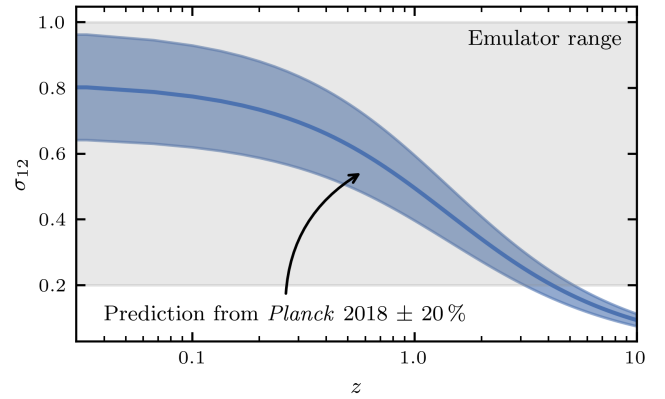


Figure 1. Prediction of σ_{12} as a function of redshift using the *Planck* 2018 TT,TE,EE+lowE+lensing best-fit cosmological parameters. The blue shaded band represents a 20% variation around that prediction, while for comparison the supported range of values for σ_{12} in our emulator COMET is shown as the grey shaded area.

The growth rate and σ_{12} capture the dependence on redshift and an arbitrary set of evolution parameters⁸, and therefore require a more generous support. Nonetheless, the limits on f and σ_{12} impose restrictions on the range of redshifts for which our emulator can be used. In case of the growth rate the ranges can accommodate any redshift for $\omega_c \gtrsim 0.107$, while for the most extreme values of the allowed shape parameters the lower boundary imposes the limitation $z \gtrsim 0.1$. Tighter restrictions on the supported redshifts come from the range of σ_{12} and to demonstrate that we compare them in Fig. 1 against the *Planck* prediction of σ_{12} as a function of redshift using the best-fit cosmological parameter values from *Planck Collaboration et al. (2020)*. When exploring cosmological parameters using a large-scale structure likelihood function, they will give rise to values of σ_{12} that are typically close (within $\sim 10\%$) to the *Planck* prediction, while the $1\text{-}\sigma$ uncertainty on σ_{12} is of the order 5% for constraints from the BOSS galaxy survey (*Semenaite et al. 2022*). To account for these uncertainties we plot a 20% error band around the *Planck* prediction in Fig. 1 and expect that any sampled cosmological parameters will correspond to σ_{12} values falling roughly into that range. We see that this band leaves the σ_{12} range of our emulator at a redshift $z \sim 3$, which means that COMET is no longer guaranteed to provide accurate predictions beyond that redshift.

3.4.2 Generation of training data sets

We generate two separate training sets, one spanning the full parameter space intended for the ratios $\beta_{\mathcal{B},\ell}$, and another covering only the shape parameters for the remaining quantities. Both training sets are built by drawing a number of samples from a Latin Hypercube, using 1500 and 750 samples, respectively. In order to obtain an optimal coverage of the parameter spaces we repeat the sampling step 10,000 times and pick the set which maximises the minimum (Euclidean) distance between any two of its points. We then evaluate all of the model ingredients using a numerical integrator and starting from CAMB-generated linear input power spectra. Before training the emulator we perform one additional pre-processing step, in which we further reduce the dynamical range of the training data by taking the logarithm and in which we normalise each component, such that it has zero mean and unit variance over the full set of samples.

⁸ In our current release of COMET we allow to specify values for h , A_s , ω_K , w_0 , and w_a .

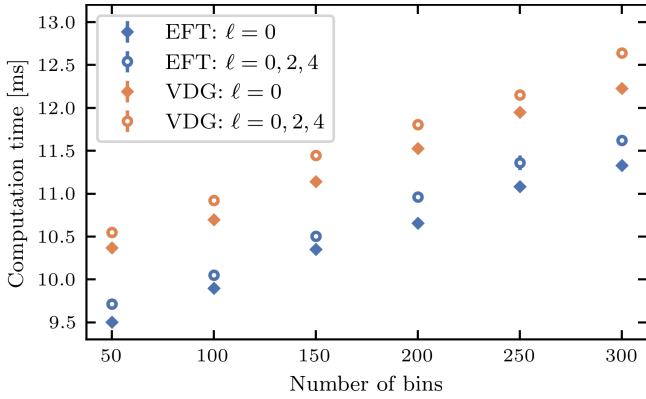


Figure 2. Computation time as a function of the provided number of bins for the EFT and VDG models, either for the monopole alone, or all three multipoles.

3.4.3 Gaussian process emulation

For the actual emulation step we employ Gaussian Processes (GP), whose properties are discussed in detail in [Rasmussen & Williams \(2006\)](#). The crucial ingredient in a GP model is the kernel function $K(\mathbf{x}, \mathbf{x}')$, which describes the covariance between two points \mathbf{x} and \mathbf{x}' of the training set. Due to a lack of knowledge about the precise functional form of this covariance we generated emulators with different combinations of commonly used kernel functions in the literature. After comparing their performance we settled on the following kernel function

$$K(\mathbf{x}, \mathbf{x}') = K_{\text{exp}}(\mathbf{x}, \mathbf{x}') + K_{3/2}(\mathbf{x}, \mathbf{x}'), \quad (49)$$

which is a combination of a squared exponential kernel,

$$K_{\text{exp}}(\mathbf{x}, \mathbf{x}') = \exp\left(-\frac{r^2}{2}\right), \quad (50)$$

and a Matérn kernel of degree $\nu = 3/2$,

$$K_{3/2}(\mathbf{x}, \mathbf{x}') = \left(1 + \sqrt{3}r\right) \exp\left(-\sqrt{3}r\right), \quad (51)$$

where $r^2 = \sum_{i=1}^d (x_i - x'_i)^2 / l_i^2$ and d is the dimension of the parameter space. The quantities l represent so-called hyperparameters, which characterise the length scales of typical features in the training data and they can differ between the two kernel functions. The values of these hyperparameters are optimised by maximising the log-likelihood of our GP models with respect to the training data. We implement this procedure using the publically available package GPy and repeat the optimisation step five times with different random initialisations, selecting for each emulator the parameter set that provides the largest log-likelihood.

3.5 Computational performance

In this section we measure the execution times of COMET for the two different RSD models, each for a different number of multipoles and number of scales. The computational performance will of course depend on the given platform, so the reader should keep in mind that all measurements reported here are based on a laptop equipped with an Apple M1 Pro processor, using one CPU (up to 3.22 GHz) and a single thread.

We measure the execution times using the function `perf_counter` from Python’s `time` module and in order to reduce uncertainties,

Table 3. Parameters included in the Λ CDM validation set and their minimum and maximum values. The parameter a_{vir} is only included in the validation set for the VDG model and its minimum and maximum values are given in units of h^{-1} Mpc.

Parameter	Minimum	Maximum
ω_b	0.02100	0.02365
ω_c	0.095	0.145
n_s	0.93	1.00
h	0.55	0.85
A_s	0.8	3.0
a_{vir}	0.0	8.0

we repeat the prediction of the power spectrum multipoles N_{exec} times for values of N_{exec} ranging from 1 to 35. We then fit a straight line to the resulting measurements as a function of N_{exec} , such that the slope of that line provides a robust estimate (and uncertainty) of the execution time per call. In Fig. 2 we plot these estimates for a varying number of scales spaced logarithmically between $k_{\text{min}} = 0.001 \text{ Mpc}^{-1}$ and $k_{\text{max}} = 0.35 \text{ Mpc}^{-1}$ for the EFT model in blue and the VDG model in orange. Filled symbols in each case correspond to the prediction of only the monopole, while open symbols also include the computation of the quadrupole and hexadecapole. We see that the execution times range from ~ 9.5 ms to ~ 11.5 ms for 50 to 300 bins in case of the EFT model. The VDG model takes on average about 1 ms longer, due to the integration over μ also involving the evaluation of the effective damping function W_{∞} . On the other hand, we see little difference between a prediction of just the monopole, or all three multipoles, since for the reconstruction of the anisotropic power spectrum the emulator of all three multipoles need to be called in any case.

Considering that the execution time for other public codes, such as CLASS-PT ([Chudaykin et al. 2020](#)) or PyBird ([D’Amico et al. 2021](#)) is of the order ~ 1 s (based on a timing estimate given by the authors of the former code, but using more than one CPU), COMET achieves a speed-up of at least two orders of magnitude.

4 VALIDATION OF THE EMULATOR

In this section we perform a number of mock analyses based on synthetic data sets at multiple redshifts using statistical uncertainties corresponding to a volume ten times larger than that expected for the *Euclid* galaxy survey. These analyses not only allow us to determine the relative uncertainties introduced by the emulator, they also — and this is of much greater relevance — let us test how these uncertainties propagate to the posteriors of cosmological and galaxy bias parameters.

4.1 Generation of synthetic validation data

4.1.1 Λ CDM validation set

Our main validation sample consists of a set of flat Λ CDM cosmologies covering the parameters ω_b , ω_c , n_s , h , and A_s for the EFT model, while for the VDG model we also include a_{vir} . Each validation set is generated by drawing 1500 random points within these five-, or six-dimensional parameter spaces, satisfying only the minimum and maximum values given in Table 3. For each point in the validation set we compute the power spectrum multipoles using the exact model at the four redshifts $z = 0.9, 1.2, 1.5,$ and 1.8 , and making the following assumptions for the galaxy bias parameters: we

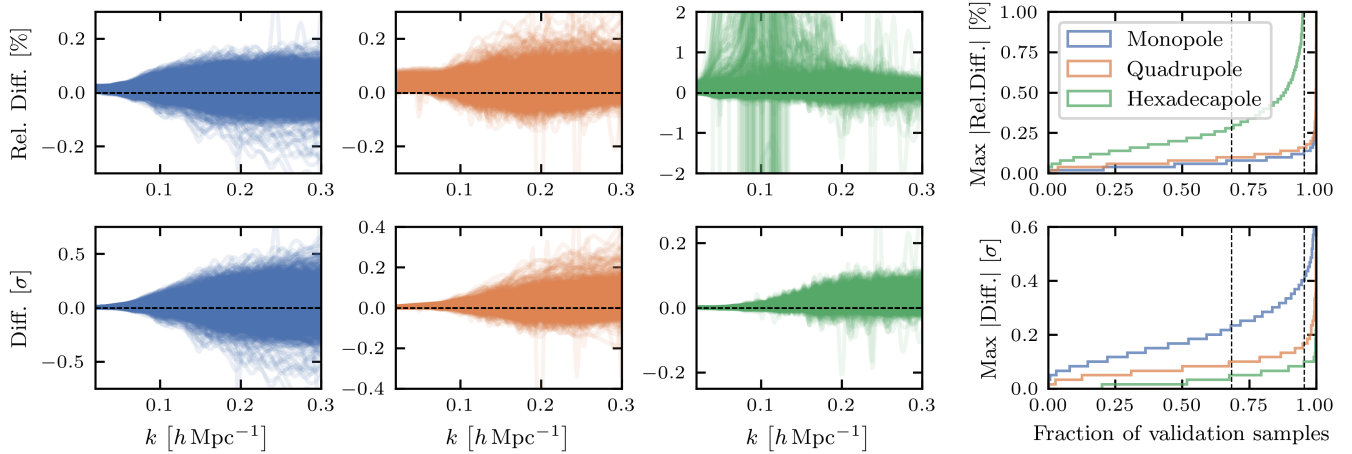


Figure 3. Inaccuracies of the emulated multipoles as a function of scale for the EFT model at $z = 0.9$. Differences are shown in percent (upper panels) and in units of the standard deviation of our synthetic data set (covering 10 times the volume of a *Euclid* redshift shell, see Sec. 4.1.1; lower panels) for all cosmologies of the validation set and using a combination of bias parameters from a random point in each chain. The fourth panel shows the cumulative histogram of the maximum absolute differences over the full range of scales with the two vertical dashed lines indicating 68% and 95% of the validation samples.

fix the value of the linear bias using $b_1(z) = \sqrt{1+z}$, which provides a reasonable estimate of the bias of $H\alpha$ galaxies to be selected by *Euclid* (Rassat et al. 2008; di Porto et al. 2012), whereas for γ_2 we impose the excursion-set relation of Sheth et al. (2013); Eggemeier et al. (2020). We then determine the values of b_2 and γ_{21} according to the peak-background-split and coevolution relations from Lazeyras et al. (2016) and Eggemeier et al. (2019), respectively, as functions of b_1 and γ_2 , and set all other counterterm and stochastic model parameters to zero. Each of the synthetic multipoles accounts for Alcock-Paczynski distortions in an exact manner (i.e., not via the approximation discussed in Sec. 3.3.1), based on a fiducial flat Λ CDM cosmology at the same redshifts as the predictions and with fixed parameters $h = 0.67$ and $\omega_m = \omega_c + \omega_b = 0.1432$.

In a second step we construct statistical uncertainties for these synthetic measurements by adopting Gaussian covariances matrices, which are computed from the synthetic multipoles at each point in the validation set using the expressions given, for instance, in Grieb et al. (2016). In order to relate these uncertainties to the characteristics of the *Euclid* survey, we further assume tracer densities that match the number densities of $H\alpha$ galaxies in the *Euclid* Flagship I mock catalogues (see Table C1), as well as *Euclid*-like volumes. The latter are derived from redshift shells of width $\Delta z = 0.2$, centred on the respective redshifts for which the power spectrum multipoles have been evaluated, and covering a sky area of $15,000 \text{ deg}^2$. To increase the stringency of our validation tests, we then multiply these volumes by a factor of 10, which is equivalent with a reduction of the statistical uncertainties by a factor of ~ 3 .

We stress that the various choices in generating this synthetic data set are not meant to provide power spectrum measurements that closely mimic those of any real galaxy samples. Nonetheless, we expect the relative uncertainties, σ_ℓ/P_ℓ , to be well representative (apart from the stringency volume factor) for *Euclid*, such that we can make a meaningful assessment of the performance of our emulator.

4.1.2 Synthetic measurements for fixed set of parameters

For a further validation test we generate one more set of synthetic power spectrum multipoles at fixed cosmological and bias parameters. We compute the power spectrum multipoles from the exact model (in this case only for the EFT) at the same four redshifts as

before, but using the bias parameter values for $b_1, b_2, \gamma_{21}, c_0, c_2, c_4, c_{\text{nlo}}$ and N_0^P given in Table C1. The value for γ_2 is again fixed in terms of the excursion set relation, while the cosmological parameters at all four redshifts are set to $h = 0.67, \omega_c = 0.1212, \omega_b = 0.021996, n_s = 0.96$ and $A_s = 2.11065$. As described in Sec. 4.1.1 we then derive statistical uncertainties for these synthetic measurements in the Gaussian approximation, using the number densities specified in Table C1 and volumes that correspond to the same redshift shells as above, including the stringency factor of 10.

4.2 Results across Λ CDM validation set

Our goal is to quantify the impact of the emulation inaccuracies on mean parameter values and their uncertainties, when performing a full likelihood exploration using all three galaxy power spectrum multipoles. To that end we use the synthetic data vectors and covariance matrices described in Sec. 4.1.1 and for each combination of cosmological parameters in the validation set we run two Monte Carlo Markov chains⁹ (MCMC), one with the exact theory model, the other using the emulator predictions. In those chains we keep the cosmological parameters fixed, while varying a set of seven bias parameters: b_1, b_2, γ_{21} , the constant shot noise N_0 , as well as the three counterterm parameters c_0, c_2 , and c_4 ; γ_2 is fixed in terms of the aforementioned excursion set relation as a function of b_1 . We pick a maximum wavenumber of 0.3 h Mpc^{-1} for all three multipoles in this analysis, which means that any significant deviations between the true and emulated models up to that scale can lead to shifts between the posterior mean values recovered from the two chains, as well as to differences in the credible regions.

4.2.1 Relative inaccuracies

Before identifying the effects on the parameter constraints, let us first consider the relative differences between the exact model and

⁹ These chains are run with emcee (Foreman-Mackey et al. 2013), using 32 walkers and for a number of steps at least ten times the maximum auto-correlation length for all varied parameters. The chains are then post-processed with getdist (Lewis 2019) in order to extract posteriors and related statistics.

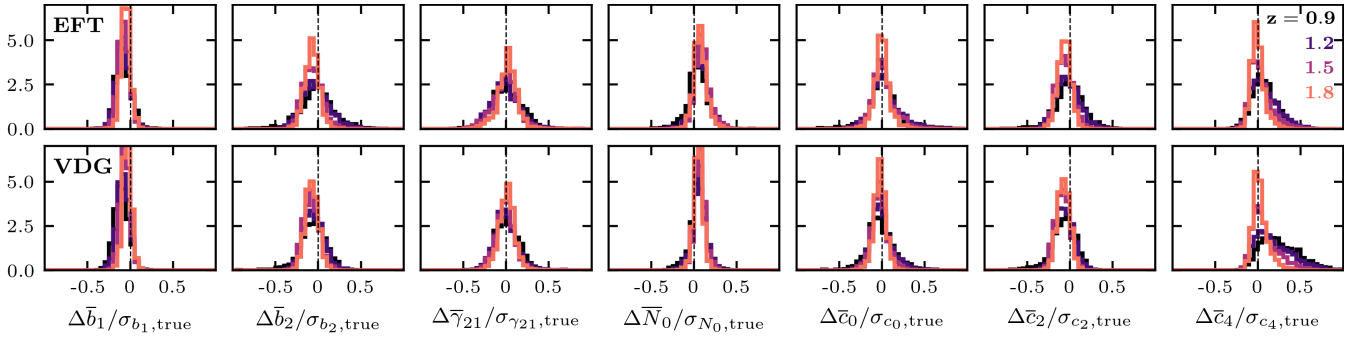


Figure 4. Distributions of the differences between the posterior mean values obtained from running MCMC with the exact and emulated model predictions. Chains were run for synthetic data including the monopole, quadrupole and hexadecapole up to $k_{\max} = 0.3 h \text{ Mpc}^{-1}$ with uncertainties corresponding to expected errors for the *Euclid* survey (see Sec. 4.1.1), but with ten times larger volumes. Each column shows the distribution for a different parameter varied in the chain in units of the respective standard deviation extracted from the chain using the true model, while the two different rows correspond to the different RSD models. The transition from dark to bright colours indicates increasing redshifts.

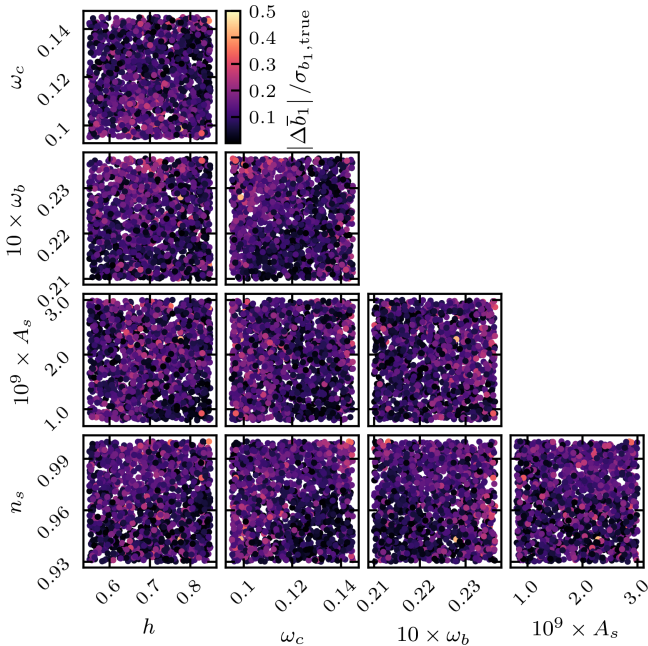


Figure 5. Shifts in the posterior means of b_1 between the true and emulated EFT model at $z = 0.9$. Each panel shows a scatter plot of all validation samples, projected into different parameter planes.

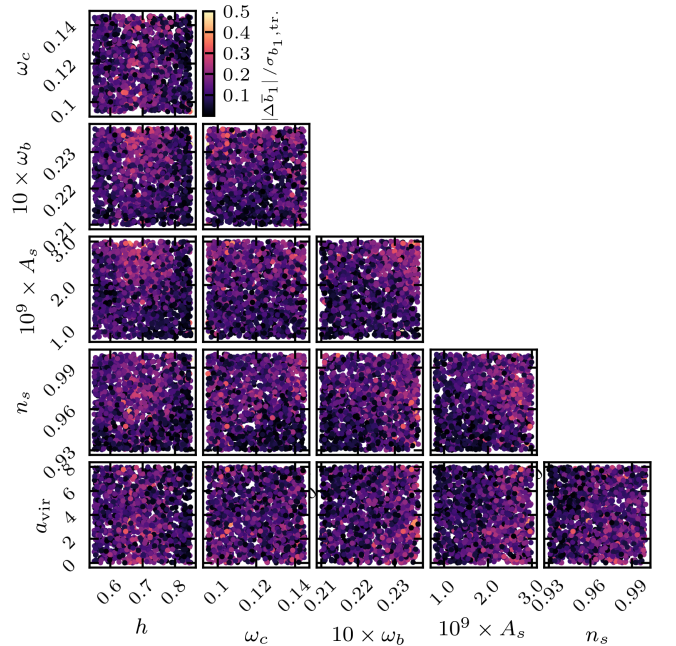


Figure 6. Same as Fig. 5, but for the VDG model at $z = 0.9$.

the emulator as a function of scale. These are shown exemplarily for the EFT model at $z = 0.9$ in the upper panels of Fig. 3, where each line has been evaluated for a different point in the validation set and a randomly selected point from the chain over bias parameters that was run for the exact model. We see that the relative differences for the monopole (blue) and quadrupole (orange) grow between $k = 0.1 h \text{ Mpc}^{-1}$ and $0.2 h \text{ Mpc}^{-1}$, after which they saturate and generally stay below the 0.2% threshold. This can be seen more clearly in the cumulative histogram in the fourth panel, which plots the maximum of the absolute relative difference over all scales and shows that there is only a vanishingly small fraction of cosmologies in the validation data sets that gives rise to discrepancies larger than 0.2%. In fact, we find that 68% of all validation samples have maximum uncertainties smaller than 0.08% and 0.1% for the monopole and quadrupole, respectively. The situation is slightly worse for the hexadecapole, where for the same fraction of validation samples the

maximum differences are only below 0.3%, but this is mostly due to the hexadecapole crossing zero for many of the tested cosmologies. It is more meaningful to plot these differences in units of some estimate of the measurement uncertainties, and for the results in the lower panels of Fig. 3 we have picked the standard deviations taken from the covariance matrices discussed in Sec. 4.1.1. We now obtain the reversed picture: due to the monopole having the smallest uncertainties, its differences appear larger than for both, the quadrupole and hexadecapole, so it will dominate the impact on any parameter posteriors. However, 68% of the validation samples still have a maximum difference smaller than 0.24σ at 10 times the *Euclid* volume for this redshift shell. The analogous results for the VDG model and the other redshifts are qualitatively very similar — we only note that the differences in units of the measurement uncertainties decrease with increasing redshift because of the decreasing tracer number densities and thus a larger contribution from shot noise, see Appendix C.

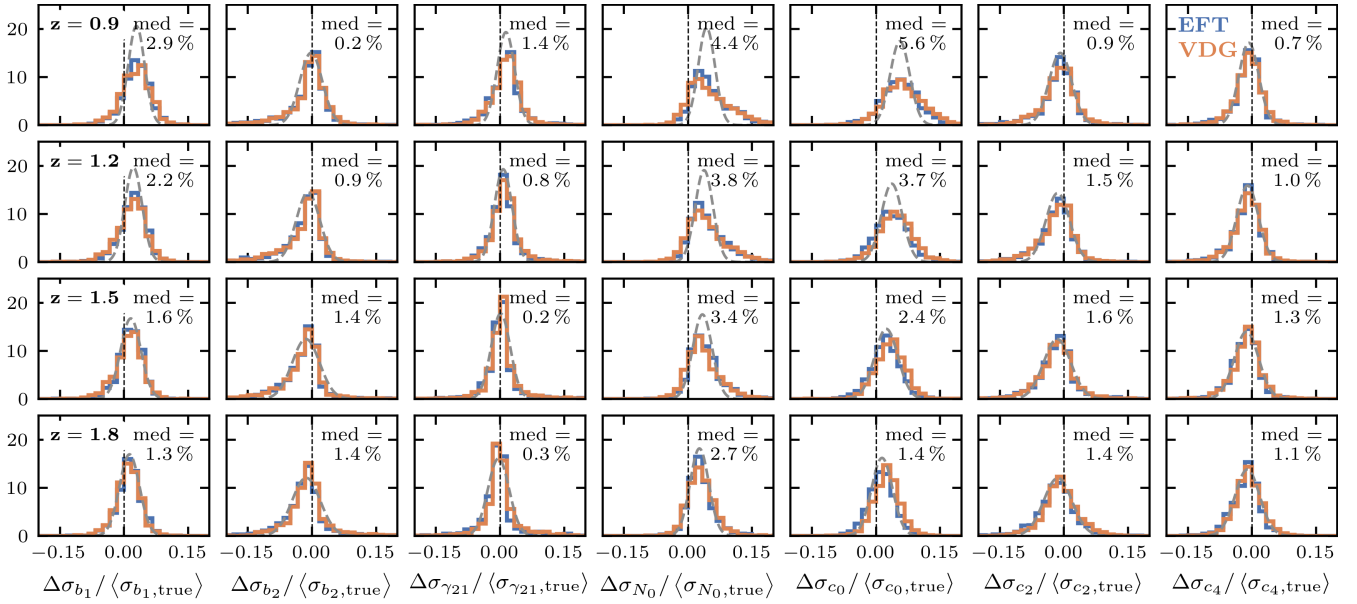


Figure 7. Histograms of the differences in the 68% credible regions between the true and emulated models, normalised by the average 1- σ constraints obtained from the true model of all validation samples, $\langle\sigma_{X,\text{true}}\rangle$. Each column depicts a different parameter varied in the chains, while each row shows a different redshift of the synthetic data set; the two different colours correspond to the two RSD models. The grey dashed lines are Gaussian distributions, centred on the median value of the EFT histograms, and represent an estimate of the spread due to sampling noise alone (see text for details).

4.2.2 Shifts in posterior means

In order to study the impact of these inaccuracies on the parameter posteriors, we extract the 1d-marginalised posterior means for each of the seven bias parameters from the two chains and compute their difference in units of the 1- σ parameter uncertainty obtained from the chain using the exact model, $\sigma_{X,\text{true}}$ (with X denoting any of the seven bias parameters). Fig. 4 shows the resulting histograms over the full validation set for all four redshifts and both of the RSD models. We clearly see that none of these cases produces any significant shifts in the varied parameters. More precisely, the means of the distributions stay consistently below $0.1 \sigma_{X,\text{true}}$, while the standard deviations reach a maximum of $0.2 \sigma_{X,\text{true}}$, showing that for the majority of the validation cosmologies we recover the true posterior means with high accuracy, while even the largest shifts remain negligible for the nominal *Euclid* volume. The parameters b_1 and N_0 generally display the smallest shifts, since they already get well constrained by the large-scale power spectrum, where the emulation inaccuracies are smallest. The higher-order bias parameters b_2 and γ_{21} , as well as the counterterm parameters, on the other hand, are mostly constrained from the non-linear regime, such that they are more susceptible to the slightly larger emulation errors for k -modes beyond $0.2 h \text{ Mpc}^{-1}$. The largest shift (with a mean value of $\sim 0.25 \sigma_{X,\text{true}}$) occurs for c_4 in case of the VDG model at $z = 0.9$. As we will show in Sec. 4.4, this is because the VDG model is more heavily affected by inaccuracies from the reconstruction of the anisotropic power spectrum and these inaccuracies are most notable for the small-scale hexadecapole. Since c_4 is mainly constrained by the hexadecapole, it absorbs these mismatches, resulting in the larger shifts. Finally, we note that the standard deviations for the distributions of the shifts are a little smaller than the value of the maximum difference (in units of σ) for 68% of the samples found in Sec. 4.2.1, but they are generally consistent, suggesting that the latter can serve as a good indicator for the performance of the emulator in explorations of the likelihood.

It is instructive to check whether the largest inaccuracies from the emulator occur dominantly in certain parts of the cosmological

parameter space. For that reason in Figs. 5 and 6 we plot the shifts in the linear bias parameter for the EFT and VDG models at $z = 0.9$, respectively, using all two-dimensional projections of the validation parameter set. We see indeed that for certain parameter combinations larger shifts (lighter colours) do not appear randomly, but in well separated regions: for instance, for the EFT model the most obvious separation occurs in the $\omega_b - \omega_c$ parameter plane, showing that there are larger inaccuracies for large values of ω_b and simultaneously small values of ω_c . A similar trend can also be observed for the VDG model, in which case there is an additional tendency for larger shifts in the $\omega_b - A_s$ parameter plane. We obtain similar results for the other redshifts, emphasising that in central regions of the parameter space, in particular for values of ω_b close to the *Planck* or Big Bang Nucleosynthesis priors, where one would preferentially sample the cosmological likelihood, the emulator performs best.

4.2.3 Impact on credible regions

Finally, let us consider how well we can recover the 1- σ credible regions for the parameters varied in the chains. This is more difficult to quantify precisely because, unlike the posterior means, the credible regions are more heavily affected by sampling noise, i.e., they carry a stronger dependence on the initial seed used for the MCMC at fixed convergence criterion. Ideally, we would therefore first quantify the sampling noise for each point in the validation set by running multiple chains with different initial seeds and constructing probability distributions of the 1- σ credible region for each parameter, which could be compared between the exact and emulated models. However, as that procedure is very costly due to the need of running many individual chains, we settle on an approximate comparison only.

First we assume that the sampling noise is independent of cosmology and that the values of the 1- σ confidence limits for each bias parameter are drawn from Gaussian distributions with means $\bar{\sigma}_{X,\text{true/emu}}(\Theta)$ and variance $\sigma_{X,\text{true/emu}}^2$, where Θ denotes the dependence on cosmological parameters contained in the validation set.

The difference in the estimated 1- σ confidence limits between the true and emulated models is then also Gaussian distributed with mean $\bar{\sigma}_{X,\text{emu}}(\Theta) - \bar{\sigma}_{X,\text{true}}(\Theta) = \Delta\bar{\sigma}_X(\Theta)$ and variance $2\sigma_{X,\text{sampling}}^2$. In the case that $\Delta\bar{\sigma}_X(\Theta)$ is small or has negligible dependence on cosmology, we can regard each value $\Delta\sigma_X$ obtained at a different validation cosmology as being independently drawn from the same sampling noise distribution and we can interpret the offset of that distribution from zero mean as the accuracy with which we can recover the 1- σ credible regions. On the other hand, if $\Delta\bar{\sigma}_X(\Theta)$ strongly depends on cosmology, the distribution of $\Delta\sigma_X$ values over the validation set will be broader and/or have a different shape, and so we cannot immediately assess the significance of the differences in σ_X from the data we have generated.

In Fig. 7 we plot the distributions of $\Delta\sigma_X$, normalised by the average over the entire validation set, $\langle\sigma_{X,\text{true}}\rangle$, for the two RSD models and the four different redshifts. In order to quantify the sampling noise we pick a Λ CDM cosmology with parameter values corresponding to the *Planck* 2018 TT,TE,EE+lowE+lensing constraints, for which we run 1000 chains with the exact predictions for the EFT and VDG models at each redshift, and varying the same seven bias parameters as before, but with different initial seeds. We then determine $\sigma_{X,\text{sampling}}^2$ in each case by fitting a Gaussian to the resulting distributions of $\sigma_X/\langle\sigma_X\rangle - 1$, where $\langle\sigma_X\rangle$ is the average of σ_X over the 1000 different chains. This allows us to plot the reference sampling noise distributions (grey dashed lines in Fig. 7) as Gaussians with variance $2\sigma_{X,\text{sampling}}^2$ and mean given by the median of the EFT distributions (blue histograms).

From these plots we observe that many of the histograms over the validation set are indeed consistent with sampling noise and moreover, in those cases the differences between $\sigma_{X,\text{true}}$ and $\sigma_{X,\text{emu}}$ are at the per-cent level, which is insignificant compared to the spread due to sampling noise. Some parameters, in particular b_1 , N_0 , and c_0 , display broader or skewed distributions, suggesting that in those cases the cosmology dependence of the differences of σ_X is stronger. In those cases we can only deduce that on average the differences are still at the per-cent level (see median values), but it is not possible to judge their significance. The deviations from the sampling noise distributions are largest at $z = 0.9$, where the synthetic measurements uncertainties are smallest and hence where the emulation inaccuracies carry the strongest weight, while going to $z = 1.8$ gives again very good consistency with sampling noise for all parameters. We do not find any significant differences between the two RSD models.

4.3 Results for analysis with varying cosmological parameters

Finally, we analyse the synthetic power spectrum multipoles described in Sec. 4.1.2. As before, we run two chains, one with the exact model, the other using COMET, but instead of keeping the cosmological parameters fixed as in the previous section, we now also vary h , ω_c and A_s , setting only n_s and ω_b to their fiducial values. Out of the full set of bias parameters we include b_1 , b_2 , γ_{21} , c_0 , c_2 , c_4 , and N_0 in the chains, fixing γ_2 and $c_{\text{nl}0}$ to the values used in the generation of the synthetic data. Since explorations of the likelihood with varying cosmological parameters is much more computationally expensive for our exact model code, we limit ourselves here to only a single case per redshift.

The chains are run using MultiNest (Feroz & Hobson 2008; Feroz et al. 2009, 2019) with 1800 live points in case of COMET and a standard Metropolis-Hastings sampler with a total number of 42,000 accepted steps in case of the exact model. After processing these chains with *getdist* (Lewis 2019) we obtain the 2d marginalised

posteriors for the full set of parameters at redshift $z = 0.9$ shown in Fig. 8, where the results based on the exact model correspond to the blue contours, the ones based on COMET to the orange contours. We see that the agreement between the posteriors of the two models is close to perfect: the mean posterior values of all parameters are almost identical and any occurring shifts are well below the 1- σ level, while the 1- σ and 2- σ credible regions are equally well recovered. Some slight differences can be observed in the tails of the posterior distributions, but these are most sensitive to the sampling routines and therefore most likely caused by differences in the two samplers used here. Although not shown, we find qualitatively very similar results at the three remaining redshifts, so that these findings confirm our results from Sec. 4.2 at fixed cosmology.

4.4 Reconstruction of anisotropic power spectrum

In this section we report the impact of inaccuracies caused by reconstructing the full anisotropic power spectrum from the monopole, quadrupole and hexadecapole only, as well as the approximate inclusion of the $\ell = 6$ multipole discussed in Sec. 3.3.1. To that end we make again use of the validation set described in Sec. 4.1.1 and compute the first three multipoles for each validation cosmology using the exact model (i.e., without any input from the emulator), but without inclusion of Alcock-Paczynski distortions and, in case of the VDG model, without the FoG damping term. Like for our emulator, we then reconstruct the anisotropic power spectrum from those multipole moments, apply Alcock-Paczynski distortions and FoG damping, and as a final step evaluate the observed multipoles. We can compare these predictions with those that do not make use of the multipole reconstruction in order to determine the differences as a function of the cosmological parameters.

This is shown in the top row of Fig. 9, where we plot the maximum difference (taken over all scales up to $k_{\text{max}} = 0.3 h \text{ Mpc}^{-1}$) in units of the synthetic standard deviations for each validation point at $z = 0.9$, projected into the $h - A_s$ parameter plane. The first three panels depict these differences for the monopole to hexadecapole for EFT model, the next three for the VDG model. We note that for the EFT model there is virtually no impact on the monopole and quadrupole, even for measurement uncertainties corresponding to 10 times the volume contained in a *Euclid* redshift shell. The situation is different for the hexadecapole, where we obtain maximum differences of up to $\sim 0.5\sigma$, in particular for large and small values of h . On the other hand, for the VDG model the effect is noticeably larger with maximum differences going well beyond 0.5σ for the hexadecapole (up to $\sim 2.5\sigma$) and also more significant inaccuracies for the monopole and quadrupole, preferentially for large values of h and A_s . This happens because the FoG damping factor carries a significant additional line-of-sight dependence, which amplifies the contributions from higher multipole moments not included in the reconstruction.

The lower panels of Fig. 9 shows how the maximum difference improve when the $\ell = 6$ multipole, evaluated at fixed shape parameters corresponding to the *Planck* 2018 TT,TE,EE+lowE+lensing values, is included in the Legendre expansion. We see that even when using this approximation the inaccuracies are significantly reduced for both RSD models. Specifically, they now stay below $\sim 0.2\sigma$ for the hexadecapole of the EFT model, while only about 5% of the validation samples reach maximum difference larger than $\sim 0.2\sigma$ and 0.35σ for the quadrupole and hexadecapole of the VDG model, respectively. Returning to the larger shifts in the counterterm parameter c_4 that we noticed in Sec. 4.2.2 for the VDG model, we find that they depend on cosmology in a very similar way as the differences in the bottom right panel of Fig. 9, implying that these shifts are caused

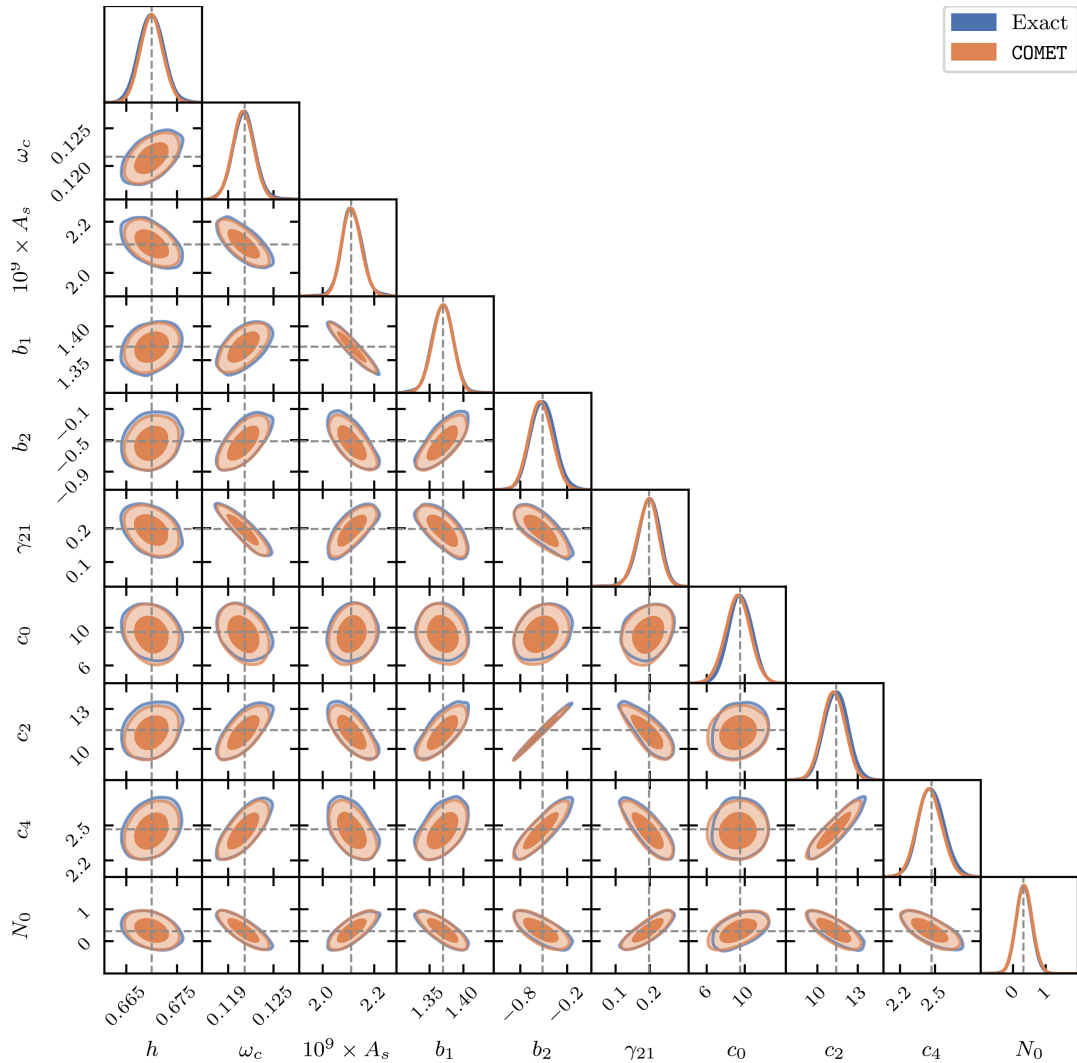


Figure 8. Comparison of the 2d and 1d marginalised posteriors obtained from running MCMC with the exact model and COMET for the EFT. The results shown stem from the synthetic data set at redshift $z = 0.9$, as described in Sec. 4.1.2 and using a volume corresponding to 10 times the volume of a *Euclid* redshift shell. The value of γ_2 was constrained to the excursion set relation of Eggemeier et al. (2020), while c_{nlo} was fixed to the fiducial value (see Table C1). The three counterterm parameters c_0 , c_2 and c_4 are given in units of $(h^{-1} \text{Mpc})^2$. Vertical and horizontal dashed lines indicate the fiducial parameter values.

by the remaining reconstruction inaccuracies in the hexadecapole. However, we stress that these are not only negligible, they also occur in a region of the cosmology parameter space that is not relevant for likelihood explorations.

5 CONCLUSIONS

5.1 Summary

We have presented COMET, an emulator of the galaxy power spectrum multipoles in redshift-space based on two different perturbation theory models: the EFT model as employed in the analyses of Ivanov et al. (2020); d’Amico et al. (2020), which fully expands the real- to redshift-space mapping, and the VDG model, which models the impact of small-scale velocity differences via a non-perturbative damping function (Scoccimarro 2004; Taruya et al. 2010; Sánchez et al. 2017). The leading idea that was driving the design of our emulator was to minimise the emulation parameter space, in order to reach an optimal compromise between computation time and accuracy.

For that reason we have adopted the evolution mapping approach of Sánchez et al. (2022) and trained COMET internally in units of Mpc over the range 0.0007Mpc^{-1} to 0.35Mpc^{-1} using only the shape parameters ω_b , ω_c , n_s , in addition to σ_{12} and the growth rate f . In this way we are able to support a broad set of evolution parameters, specifically h , A_s , Ω_K , w_0 , and w_a , by mapping them to the corresponding values of σ_{12} and f at any given redshift (up to an upper limit of $z \sim 3$, imposed by our chosen range for σ_{12}). Furthermore, we emulate all independent contributions that arise from the galaxy bias expansion separately, which precludes the associated parameters from the emulator parameter space, and apply AP distortions and the effective damping function in case of the VDG model in a separate step. This gives COMET the flexibility to support any fiducial background cosmologies and arbitrary functional forms of the damping term. A single evaluation of the monopole, quadrupole and hexadecapole at $\mathcal{O}(100)$ scales takes about 10 ms when executed on a single CPU.

Using a series of validation tests, we verified that COMET does not introduce any relevant loss in accuracy in comparison to the exact

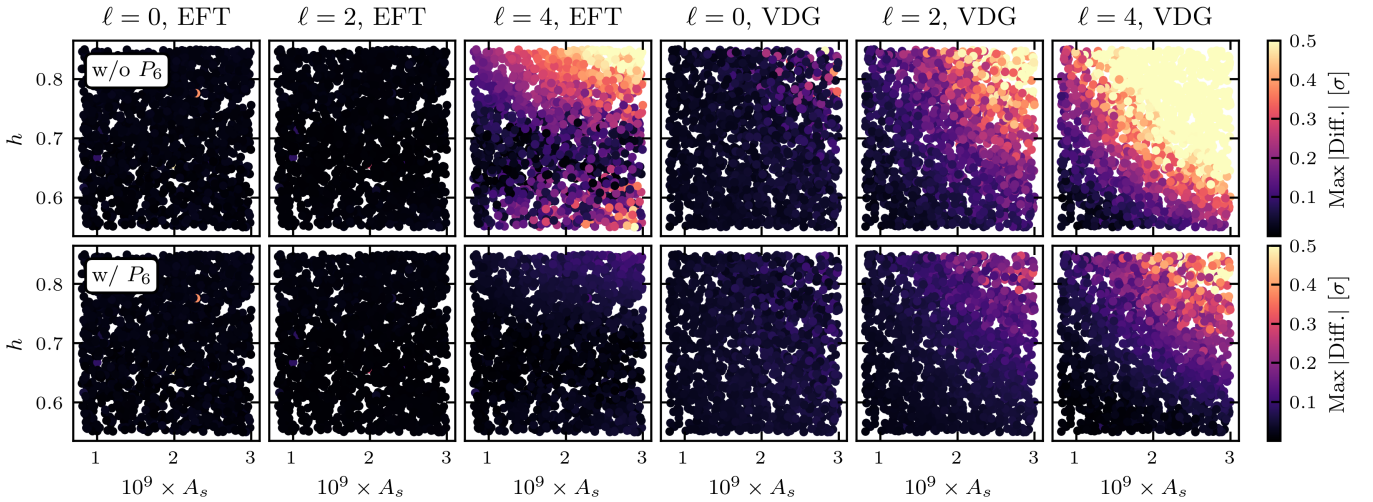


Figure 9. Maximum differences up to $k_{\max} = 0.3 h \text{ Mpc}^{-1}$ (in units of the standard deviation of our synthetic data set, see Sec. 4.1) for each point of the validation set between the exact computation of the power spectrum multipoles and when the anisotropic power spectrum before application of Alcock-Paczynski distortions and FoG damping is obtained from a Legendre decomposition truncated at finite order. In the top row the latter is based on the first three non-zero multipoles, while in the bottom row we include the $\ell = 6$ multipole moment evaluated at fixed shape parameters (see Sec. 3.3.1 for details). Both sets of predictions are generated without any input from the emulator.

perturbation theory models. We constructed a large validation set consisting of 1500 synthetic power spectrum measurements at four different redshifts between $z = 0.9$ and $z = 1.8$, covering the five-dimensional cosmological parameter space: ω_b , ω_c , n_s , h and A_s . Adopting a fixed set of galaxy bias parameters at each redshift and in case of the EFT model, we find that the relative inaccuracies stay below 0.08(0.14)%, 0.11(0.17)% and 0.30(1.33)% for 68(95)% of the validation samples and the monopole, quadrupole, and hexadecapole, respectively, up to $k_{\max} = 0.3 h \text{ Mpc}^{-1}$. We further generated statistical uncertainties for our synthetic measurements using Gaussian covariances and specifics tied to the *Euclid* survey, but with a tenfold increase in volume. In units of these uncertainties the emulation errors are below 0.24(0.42) σ , 0.10(0.17) σ , and 0.05(0.10) σ . We then ran MCMC, varying a set of seven bias parameters both for COMET and the exact model and analysing all three synthetic multipoles for each validation sample, finding that the shifts in the mean posterior values closely match the emulation inaccuracies in units of σ . Additionally, we find that the 68% credible regions are very well recovered and any occurring differences are typically smaller than the MCMC sampling noise. For the VDG model the performance is very similar, apart from a slightly less accurate hexadecapole (see discussion in Sec. 4.4), but without negative effects on the recovery of the posteriors. Finally, we constructed one more synthetic collection of measurements (again at the same four redshifts) for a fixed set of cosmological and bias parameters, which we used to demonstrate that even when running chains over the full parameter space (including cosmological parameters) there is no appreciable difference in the resulting posterior distributions between the exact model and COMET.

While we have explicitly demonstrated that the emulator is accurate up to scales of at least $k_{\max} = 0.3 h \text{ Mpc}^{-1}$, we caution that this does not have to apply to the underlying theoretical model itself. The validity of the one-loop perturbation theory depends on the relative size of the neglected non-linear corrections, as well as the amplitude of the galaxy bias parameters, and is thus a function of redshift and the particular galaxy sample under consideration. Any application to real data must therefore be preceded by a thorough study of the model’s robustness under changes of the maximum scale cuts — a

task that is ideally suited for COMET due to its superior computational efficiency.

We leave two important extensions of COMET to forthcoming publications: Firstly, the power spectrum models for both the EFT and VDG can be easily transformed to configuration space and thus, using the same emulation techniques as presented here, we would also be able to make fast predictions of the two-point correlation function multipoles. Secondly, the new generation of galaxy surveys is expected to improve our current constraints on the masses of neutrinos, which is why it is particularly important to be able to predict galaxy clustering statistics as a function of non-zero neutrino masses, unlike we have assumed here.

5.2 Comparison to related emulators in the literature

While most galaxy clustering emulators that have been presented in the literature so far have been built from simulations and focus on the non-linear regime, there are two sets of works, which are closely related to what we have presented here and which we want to briefly compare against. In particular, [Donald-McCann et al. \(2023\)](#); [DeRose et al. \(2022\)](#) have presented two perturbation theory emulators of the galaxy power spectrum multipoles. The former, EFTEMU, is based on the PyBird code ([d’Amico et al. 2020](#)), which implements perturbation theory expressions identical to those described in Sec. 2 for the EFT model apart from slight differences in the infrared resummation procedure¹⁰ and the definition of the galaxy bias parameters (see Sec. 2.2 for a conversion), while the latter, EmulateLSS, is based on the Lagrangian perturbation theory model of [Chen et al. \(2021\)](#). Although sharing the same goal, there are a number of differences between these two emulators and COMET. On the one hand, this concerns the parameter space and the range of scales for which they provide predictions: EFTEMU supports the five cosmological parameters ω_b , ω_c , h , A_s , and n_s (i.e., it does not allow for deviations

¹⁰ A comparison between CLASS-PT ([Chudaykin et al. 2020](#)), which uses the same infrared resummation technique as discussed in Sec. 2.4, and PyBird has been presented in [Nishimichi et al. \(2020\)](#), finding very similar results.

from the equation of state of a cosmological constant or for non-flat cosmologies), and with the exception of n_s all of these have smaller ranges than in COMET. EmulateLSS is even more restrictive as it also fixes the spectral index and does not cover the full galaxy bias and counterterm parameter space, ignoring for instance the second- and third-order tidal bias parameters. Moreover, both of these emulators make predictions for a fixed fiducial background cosmology and at fixed redshifts (each new fiducial background cosmology or redshift would require generating a new set of training data) and while EmulateLSS gives predictions in the range of scales from $0.001 h \text{ Mpc}^{-1}$ to $0.5 h \text{ Mpc}^{-1}$, EFTEMU has a more limiting range with a maximum wavenumber of $0.19 h \text{ Mpc}^{-1}$. On the other hand, the prediction accuracies for the three multipoles quoted by DeRose et al. (2022) are only slightly worse than what we have determined for COMET, and also Donald-McCann et al. (2023) find a sub-percent accuracy for fixed BOSS-like galaxy bias parameters, making it comparable with COMET in this regard (albeit on a more limited range of scales). Finally, both EFTEMU and EmulateLSS use neural networks instead of Gaussian processes for the emulation procedure and their computation time therefore does not depend on the size of the training set. This leads to a better computational performance than COMET by about one order of magnitude based on the fact that both works quote a computation time of $\sim 1 \text{ ms}$ (we stress, however, that eventually the computational bottleneck will lie elsewhere, e.g. in the computation of the χ^2 or, for joint chains with the bispectrum, the computation of the bispectrum model).

The methodology discussed in Zennaro et al. (2021); Aricò et al. (2022); Kokron et al. (2021) follows the same perturbative galaxy bias expansion as presented in Sec. 2.2 (although the third order term related to the parameter γ_{21} is neglected) and they have presented emulators for the various contributions to the galaxy power spectrum based on either perturbation theory (Aricò et al. 2022) like here, or on simulations in order to extend the predictions into the non-linear regime (Zennaro et al. 2021; Kokron et al. 2021). All three works consider scales up to $1 h \text{ Mpc}^{-1}$, but cover somewhat more restrictive redshift ranges than COMET, $z_{\text{max}} = 1.5$ (Aricò et al. 2022; Zennaro et al. 2021) and $z_{\text{max}} = 2$ (Kokron et al. 2021). They also emulate over somewhat different cosmological parameter spaces: the former two also cover an eight-dimensional cosmology parameter space, but instead of Ω_K account for the neutrino mass, while in the latter they use a seven-dimensional parameter space that includes the effective number of relativistic species, but does not allow for either Ω_K or a dynamical dark energy equation of state. Moreover, they generally quote an emulation accuracy of $\sim 1\%$ — one order of magnitude larger than our findings here, but for this comparison one should bear in mind that these results carry a dependency on the nature of the validation tests. While these three works only make predictions for the galaxy power spectrum in real-space, Pellejero Ibañez et al. (2022) extends their formalism in order to account for redshift-space distortions. They show that using a halo displacement field extracted from simulations and a phenomenological finger-of-god model accounting for the velocity dispersion of satellite galaxies and satellite fraction, it is possible to recover power spectrum multipoles up to $k \sim 0.6 h \text{ Mpc}^{-1}$ that are accurate within measurement uncertainties corresponding to a volume of $3(h^{-1} \text{ Gpc})^3$.

5.3 Functionality of the COMET package

COMET is a freely available Python package (<https://gitlab.com/aegge/comet-emu>), which can be installed via pip and all required tables and emulators are downloaded automatically (re-training the emulators is not necessary). We currently provide emu-

lators for the real-space power spectrum and the redshift-space power spectrum multipoles for the EFT model¹¹. Predictions can be made using either the Mpc or $h^{-1} \text{ Mpc}$ unit systems and for either the native parameter space or for a given dark energy model. The former consists of the three shape parameters ω_b, ω_c and n_s , in combination with σ_{12} and f , while in case of the latter one needs to specify the evolution parameters h, A_s, Ω_K, w_0 and w_a at some redshift z instead of σ_{12} and f . COMET accepts an arbitrary range of scales, but for those scales outside of the range for which we trained the emulators ($k \in [0.0007, 0.35] \text{ Mpc}^{-1}$), we apply a power law extrapolation. Further features of the package include:

- the prediction of the linear matter power spectrum, with or without application of infrared resummation (BAO damping)
- the prediction of the real-space tree-level galaxy bispectrum and the tree-level galaxy bispectrum multipoles in redshift-space
- the computation of the Gaussian covariance matrices of the power spectrum and bispectrum multipoles (both, real- and redshift-space)
- the computation of the χ^2 for a given set of measurements and their covariance matrix for arbitrary k_{max} scale cuts; we also provide a functionality that drastically speeds up the χ^2 computation in case of fixed cosmological parameters (e.g., when running a chain over only galaxy bias parameters)
- the possibility to choose between different galaxy bias bases (see Sec. 2.2)
- exact treatment of discreteness and finite bin width effects for the power spectrum multipoles

More information and some tutorials can be found on the documentation pages: <https://comet-emu.readthedocs.io/en/latest/index.html>.

ACKNOWLEDGEMENTS

We thank the anonymous referee for useful comments, in particular the suggestion that led to the inclusion of Appendix B. AE is supported at the Argelander Institut für Astronomie by an Argelander Fellowship. BCQ and MC acknowledge support from the Spanish Ministerio de Ciencia e Innovación under grant PGC2018-102021-B-I00, and BCQ additionally acknowledges support from a PhD scholarship from the Secretaria d'Universitats i Recerca de la Generalitat de Catalunya i del Fons Social Europeu. AGS acknowledges the support of the Excellence Cluster ORIGINS, which is funded by the Deutsche Forschungsgemeinschaft (DFG, German Research Foundation) under Germany's Excellence Strategy - EXC-2094 - 390783311. This research made use of matplotlib, a Python library for publication quality graphics (Hunter 2007).

DATA AVAILABILITY

The data underlying this article will be shared on reasonable request to the corresponding author.

REFERENCES

Alcock C., Paczynski B., 1979, *Nature*, **281**, 358

¹¹ The VDG model will be released as part of an upcoming publication.

- Angulo R. E., Zennaro M., Contreras S., Aricò G., Pellejero-Ibañez M., Stücker J., 2021, *MNRAS*, **507**, 5869
- Aricò G., Angulo R. E., Zennaro M., 2022, *Open Research Europe*, 1
- Assassi V., Baumann D., Green D., Zaldarriaga M., 2014, *J. Cosmology Astropart. Phys.*, 2014, 056
- Baldauf T., Mirbabayi M., Simonović M., Zaldarriaga M., 2015, *Phys. Rev. D*, **92**, 043514
- Ballinger W. E., Peacock J. A., Heavens A. F., 1996a, *MNRAS*, **282**, 877
- Ballinger W. E., Peacock J. A., Heavens A. F., 1996b, *MNRAS*, **282**, 877
- Baumann D., Nicolis A., Senatore L., Zaldarriaga M., 2012, *J. Cosmology Astropart. Phys.*, 2012, 051
- Beutler F., et al., 2017, *MNRAS*, **466**, 2242
- Blas D., Garny M., Ivanov M. M., Sibiryakov S., 2016, *J. Cosmology Astropart. Phys.*, 2016, 028
- Carrasco J. J. M., Hertzberg M. P., Senatore L., 2012, *Journal of High Energy Physics*, 2012, 82
- Chan K. C., Scoccimarro R., Sheth R. K., 2012, *Phys. Rev. D*, **85**, 083509
- Chen S.-F., Vlah Z., Castorina E., White M., 2021, *J. Cosmology Astropart. Phys.*, 2021, 100
- Chudaykin A., Ivanov M. M., Philcox O. H. E., Simonović M., 2020, *Phys. Rev. D*, **102**, 063533
- Cuesta-Lazaro C., Li B., Eggemeier A., Zarrouk P., Baugh C. M., Nishimichi T., Takada M., 2020, *MNRAS*, **498**, 1175
- D'Amico G., Senatore L., Zhang P., 2021, *J. Cosmology Astropart. Phys.*, 2021, 006
- DeRose J., Chen S.-F., White M., Kokron N., 2022, *J. Cosmology Astropart. Phys.*, 2022, 056
- Dekel A., Lahav O., 1999, *ApJ*, **520**, 24
- Desjacques V., 2008, *Phys. Rev. D*, **78**, 103503
- Desjacques V., Crocce M., Scoccimarro R., Sheth R. K., 2010, *Phys. Rev. D*, **82**, 103529
- Desjacques V., Jeong D., Schmidt F., 2018a, *Phys. Rep.*, **733**, 1
- Desjacques V., Jeong D., Schmidt F., 2018b, *J. Cosmology Astropart. Phys.*, 2018, 035
- Donald-McCann J., Koyama K., Beutler F., 2023, *MNRAS*, **518**, 3106
- Eggemeier A., Scoccimarro R., Smith R. E., 2019, *Phys. Rev. D*, **99**, 123514
- Eggemeier A., Scoccimarro R., Crocce M., Pezzotta A., Sánchez A. G., 2020, *Phys. Rev. D*, **102**, 103530
- Eggemeier A., Scoccimarro R., Smith R. E., Crocce M., Pezzotta A., Sánchez A. G., 2021, *Phys. Rev. D*, **103**, 123550
- Eisenstein D. J., Hu W., 1998, *The Astrophysical Journal*, **496**, 605
- Euclid Collaboration et al., 2019, *MNRAS*, **484**, 5509
- Euclid Collaboration et al., 2021, *MNRAS*, **505**, 2840
- Feroz F., Hobson M. P., 2008, *MNRAS*, **384**, 449
- Feroz F., Hobson M. P., Bridges M., 2009, *MNRAS*, **398**, 1601
- Feroz F., Hobson M. P., Cameron E., Pettitt A. N., 2019, *The Open Journal of Astrophysics*, **2**, 10
- Foreman-Mackey D., Hogg D. W., Lang D., Goodman J., 2013, *PASP*, **125**, 306
- Giblin B., Cataneo M., Moews B., Heymans C., 2019, *MNRAS*, **490**, 4826
- Grieb J. N., Sánchez A. G., Salazar-Albornoz S., Dalla Vecchia C., 2016, *MNRAS*, **457**, 1577
- Heitmann K., Higdon D., White M., Habib S., Williams B. J., Lawrence E., Wagner C., 2009, *ApJ*, **705**, 156
- Hunter J. D., 2007, *Computing in Science and Engineering*, **9**, 90
- Ivanov M. M., Sibiryakov S., 2018, *J. Cosmology Astropart. Phys.*, 2018, 053
- Ivanov M. M., Simonović M., Zaldarriaga M., 2020, *J. Cosmology Astropart. Phys.*, 2020, 042
- Juszkiewicz R., Fisher K. B., Szapudi I., 1998, *ApJ*, **504**, L1
- Kobayashi Y., Nishimichi T., Takada M., Takahashi R., Osato K., 2020, *Phys. Rev. D*, **102**, 063504
- Kokron N., DeRose J., Chen S.-F., White M., Wechsler R. H., 2021, *MNRAS*, **505**, 1422
- Kwan J., Heitmann K., Habib S., Padmanabhan N., Lawrence E., Finkel H., Frontiere N., Pope A., 2015, *ApJ*, **810**, 35
- Laureijs R., et al., 2011, arXiv e-prints, p. arXiv:1110.3193
- Lazeyras T., Wagner C., Baldauf T., Schmidt F., 2016, *J. Cosmology Astropart. Phys.*, 2016, 018
- Levi M., et al., 2013, arXiv e-prints, p. arXiv:1308.0847
- Lewis A., 2019, arXiv e-prints, p. arXiv:1910.13970
- Matsubara T., 1999, *ApJ*, **525**, 543
- McDonald P., Roy A., 2009, *J. Cosmology Astropart. Phys.*, 2009, 020
- Mirbabayi M., Schmidt F., Zaldarriaga M., 2015, *J. Cosmology Astropart. Phys.*, 2015, 030
- Nishimichi T., D'Amico G., Ivanov M. M., Senatore L., Simonović M., Takada M., Zaldarriaga M., Zhang P., 2020, *Phys. Rev. D*, **102**, 123541
- Osato K., Nishimichi T., Bernardeau F., Taruya A., 2019, *Phys. Rev. D*, **99**, 063530
- Pellejero Ibañez M., Stücker J., Angulo R. E., Zennaro M., Contreras S., Aricò G., 2022, *MNRAS*, **514**, 3993
- Perko A., Senatore L., Jennings E., Wechsler R. H., 2016, arXiv e-prints, p. arXiv:1610.09321
- Planck Collaboration et al., 2020, *A&A*, **641**, A6
- Pueblas S., Scoccimarro R., 2009, *Phys. Rev. D*, **80**, 043504
- Rasmussen C. E., Williams C. K. I., 2006, *Gaussian Processes for Machine Learning*. MIT Press
- Rassat A., et al., 2008, arXiv e-prints, p. arXiv:0810.0003
- Sánchez A. G., 2020, *Phys. Rev. D*, **102**, 123511
- Sánchez A. G., et al., 2017, *MNRAS*, **464**, 1640
- Sánchez A. G., Ruiz A. N., Jara J. G., Padilla N. D., 2022, *MNRAS*, **514**, 5673
- Scoccimarro R., 2004, *Phys. Rev. D*, **70**, 083007
- Scoccimarro R., 2015, *Phys. Rev. D*, **92**, 083532
- Scoccimarro R., Couchman H. M. P., Frieman J. A., 1999, *ApJ*, **517**, 531
- Semenaite A., et al., 2022, *MNRAS*, **512**, 5657
- Senatore L., 2015, *J. Cosmology Astropart. Phys.*, 2015, 007
- Senatore L., Zaldarriaga M., 2014, arXiv e-prints, p. arXiv:1409.1225
- Sheth R. K., 1996, *MNRAS*, **279**, 1310
- Sheth R. K., Chan K. C., Scoccimarro R., 2013, *Phys. Rev. D*, **87**, 083002
- Taruya A., Soda J., 1999, *ApJ*, **522**, 46
- Taruya A., Nishimichi T., Saito S., 2010, *Phys. Rev. D*, **82**, 063522
- Taruya A., Nishimichi T., Bernardeau F., 2013, *Phys. Rev. D*, **87**, 083509
- Vlah Z., Seljak U., Yat Chu M., Feng Y., 2016, *J. Cosmology Astropart. Phys.*, 2016, 057
- Yuan S., Garrison L. H., Eisenstein D. J., Wechsler R. H., 2022, *MNRAS*, **515**, 871
- Zennaro M., Angulo R. E., Pellejero-Ibañez M., Stücker J., Contreras S., Aricò G., 2021, arXiv e-prints, p. arXiv:2101.12187
- Zhai Z., et al., 2019, *ApJ*, **874**, 95
- d'Amico G., Gleyzes J., Kokron N., Markovic K., Senatore L., Zhang P., Beutler F., Gil-Marín H., 2020, *J. Cosmology Astropart. Phys.*, 2020, 005
- di Porto C., Amendola L., Branchini E., 2012, *MNRAS*, **419**, 985

APPENDIX A: PERTURBATION THEORY KERNELS

In the formulation used by COMET, the perturbative term of both redshift-space models, EFT and VDG, can be written in the following way,

$$P_{gg}(k, \mu) = P_{gg, \text{SPT}}^{\text{tree}}(k, \mu) + P_{gg, \text{SPT}}^{1\text{-loop}}(k, \mu) + P_{gg}^{\text{stoch}}(k, \mu) + P_{gg}^{\text{ctr}}(k, \mu), \quad (\text{A1})$$

where the individual contribution are given by

$$P_{gg, \text{SPT}}^{\text{tree}}(k, \mu) = Z_1(k)^2 P_L(k), \quad (\text{A2})$$

$$\begin{aligned} P_{gg, \text{SPT}}^{1\text{-loop}}(k, \mu) &= P_{gg, 22}(k, \mu) + P_{gg, 13}(k, \mu) = \\ &= 2 \int_{\mathbf{q}} Z_2(\mathbf{q}, \mathbf{k} - \mathbf{q})^2 P_L(|\mathbf{k} - \mathbf{q}|) P_L(q) \\ &\quad + 6 Z_1(k) P_L(k) \int_{\mathbf{q}} Z_3(\mathbf{q}, -\mathbf{q}, \mathbf{k}) P_L(q), \end{aligned} \quad (\text{A3})$$

$$P_{\text{gg}}^{\text{stoch}}(k, \mu) = \frac{1}{\bar{n}} \left\{ N_0^P + k^2 \left[N_{20}^P + N_{22}^P \mathcal{L}_2(\mu) \right] \right\}, \quad (\text{A4})$$

$$\begin{aligned} P_{\text{gg}}^{\text{ctr}}(k, \mu) &= P_{\text{gg}}^{\text{ctr,LO}}(k, \mu) + P_{\text{gg}}^{\text{ctr,NLO}}(k, \mu) = \\ &= -2 [c_0 + c_2 \mathcal{L}_2(\mu) + c_4 \mathcal{L}_4(\mu)] k^2 P_L(k) \\ &\quad + c_{\text{nl0}} f^4 \mu^4 k^4 Z_1(\mathbf{k})^2 P_L(k). \end{aligned} \quad (\text{A5})$$

Here, the redshift-space kernels Z_n are defined as

$$Z_1(\mathbf{k}) = b_1 + f\mu^2, \quad (\text{A6})$$

$$\begin{aligned} Z_2(\mathbf{k}_1, \mathbf{k}_2) &= \mathcal{K}_2(\mathbf{k}_1, \mathbf{k}_2) + f\mu^2 G_2(\mathbf{k}_1, \mathbf{k}_2) + \\ &\quad + \frac{1}{2} f k \mu \left[\frac{\mu_1}{k_1} (b_1 + f\mu^2) + \frac{\mu_2}{k_2} (b_1 + f\mu^2) \right], \end{aligned} \quad (\text{A7})$$

$$\begin{aligned} Z_3(\mathbf{k}_1, \mathbf{k}_2, \mathbf{k}_3) &= \mathcal{K}_3(\mathbf{k}_1, \mathbf{k}_2, \mathbf{k}_3) + f\mu^2 G_3(\mathbf{k}_1, \mathbf{k}_2, \mathbf{k}_3) \\ &\quad + \frac{1}{2} f^2 k^2 \mu^2 \frac{\mu_2 \mu_3}{k_2 k_3} (b_1 + f\mu^2) \\ &\quad + f k \mu \frac{\mu_3}{k_3} \left[b_1 F_2(\mathbf{k}_1, \mathbf{k}_2) + f\mu_{12}^2 G_2(\mathbf{k}_1, \mathbf{k}_2) \right] \\ &\quad + f k \mu \frac{\mu_{23}}{k_{23}} (b_1 + f\mu^2) G_2(\mathbf{k}_2, \mathbf{k}_3) \\ &\quad + f k \mu \frac{\mu_1}{k_1} \left[\frac{b_2}{2} + \gamma_2 K(\mathbf{k}_2, \mathbf{k}_3) \right], \end{aligned} \quad (\text{A8})$$

where the $Z_3(\mathbf{k}_1, \mathbf{k}_2, \mathbf{k}_3)$ needs to be symmetrised over its arguments. The real-space galaxy kernels \mathcal{K}_n read

$$\mathcal{K}_2(\mathbf{k}_1, \mathbf{k}_2) = b_1 F_2(\mathbf{k}_1, \mathbf{k}_2) + \frac{b_2}{2} + \gamma_2 K(\mathbf{k}_1, \mathbf{k}_2), \quad (\text{A9})$$

$$\begin{aligned} \mathcal{K}_3(\mathbf{k}_1, \mathbf{k}_2, \mathbf{k}_3) &= b_1 F_3(\mathbf{k}_1, \mathbf{k}_2, \mathbf{k}_3) + b_2 F_2(\mathbf{k}_1, \mathbf{k}_2) \\ &\quad + 2\gamma_2 K(\mathbf{k}_1, \mathbf{k}_2 + \mathbf{k}_3) G_2(\mathbf{k}_2, \mathbf{k}_3) \\ &\quad + 2\gamma_{21} K(\mathbf{k}_1, \mathbf{k}_2 + \mathbf{k}_3) K(\mathbf{k}_2, \mathbf{k}_3), \end{aligned} \quad (\text{A10})$$

with

$$K(\mathbf{k}_1, \mathbf{k}_2) = \frac{(\mathbf{k}_1 \cdot \mathbf{k}_2)^2}{k_1^2 k_2^2} - 1. \quad (\text{A11})$$

The kernel $\mathcal{K}_3(\mathbf{k}_1, \mathbf{k}_2, \mathbf{k}_3)$ also needs to be symmetrised over its arguments.

APPENDIX B: BINNING AND DISCRETENESS EFFECTS IN ESTIMATES OF THE POWER SPECTRUM

The power spectrum multipoles are estimated from density grids in Fourier space by taking the square of the Fourier coefficients at each wavevector \mathbf{k} and multiplying by the respective Legendre polynomial (for more detail, see [Scoccimarro 2015](#)). These estimates are then summarised into measurements at multiple wavemode bins, k_i , by averaging over all wavevectors that fall into a spherical shell centred on k_i with some specified bin width Δk . Both, the finite bin width as well as the discreteness of the Fourier grid, introduce differences compared to the theoretical power spectrum multipoles as defined in Sec. 3, which are evaluated at fixed k and by integrating over continuous values of μ , the orientation of \mathbf{k} with respect to the line-of-sight (see e.g. Eq. 45). This can be accounted for by averaging the

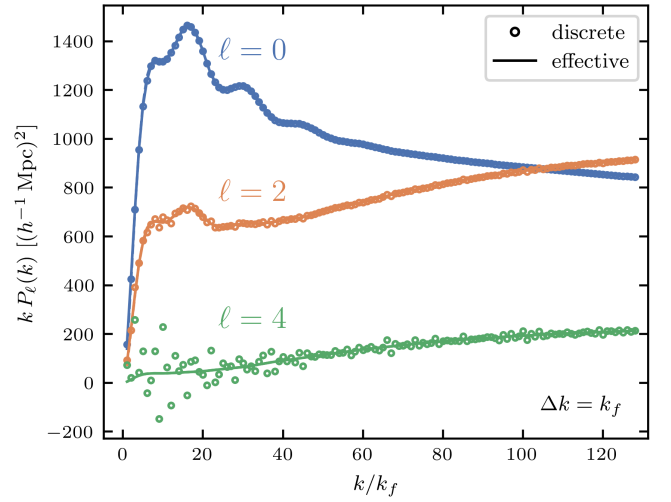


Figure B1. Comparison of the power spectrum multipole predictions evaluated at the effective wavemodes (lines) and averaged over discrete set of k and μ values Eq. (B1) (circles). The bin width was assumed to be k_f , with $k_f \approx 0.0042 h \text{ Mpc}^{-1}$.

theoretical power spectrum $P(k, \mu)$ in the same way as done for the measurements (e.g. [Taruya et al. 2013](#)). The “observed” theoretical multipoles are thus given by

$$P_\ell^{\text{obs}}(k_i) = \frac{2\ell + 1}{N_k} \sum_{|\mathbf{k}| \in [k_i - \Delta k/2, k_i + \Delta k/2]} P(k, \mu) \mathcal{L}_\ell(\mu), \quad (\text{B1})$$

where N_k are the total number of wavevectors per spherical shell.

Instead of averaging the full power spectrum, a common approximation is to evaluate the power spectrum multipoles at the *effective* wavemodes, defined as

$$k_{i,\text{eff}} \equiv \frac{1}{N_k} \sum_{|\mathbf{k}| \in [k_i - \Delta k/2, k_i + \Delta k/2]} |\mathbf{k}|, \quad (\text{B2})$$

which can partially account for the finite bin width. In Fig. B1 we compare Eq. (B1) (circles) against the power spectrum multipoles evaluated at the effective wavemodes (lines) for a Fourier grid with fundamental frequency, $k_f = 2\pi/L$, corresponding to a box size of $L = 1500 h^{-1} \text{ Mpc}$ and bin width $\Delta k = k_f$. While the discreteness effect is barely noticeable for the monopole, it already gives rise to per-cent level differences in the quadrupole, and even more significant effects in the hexadecapole. This is particularly the case for bins which are close to the fundamental frequency, where there are consequently only a small number of wavevectors per spherical shell, but for the hexadecapole differences up to $\sim 10\%$ persist up to $k \sim 100 k_f$.

We have implemented the exact bin average for arbitrary bin widths (with linear spacing) in COMET by computing Eq. (B1) over the anisotropic power spectrum reconstructed from the emulated quantities (see Sec. 3.3.1). We have verified that the reconstruction of the anisotropic power spectrum from a finite number of multipoles does not introduce any appreciable inaccuracies when performing the bin average, as was also the case without bin average (see Sec. 4.4). In order to speed up the computation of the binned predictions, we first find all discrete values of k and μ for each bin and then perform the following rounding operations

$$k \approx \left\lfloor 10 \frac{k}{\Delta k} \right\rfloor \frac{\Delta k}{10}, \quad (\text{B3})$$

$$\mu \approx 10^{-3} \left\lfloor 10^3 \mu \right\rfloor, \quad (\text{B4})$$

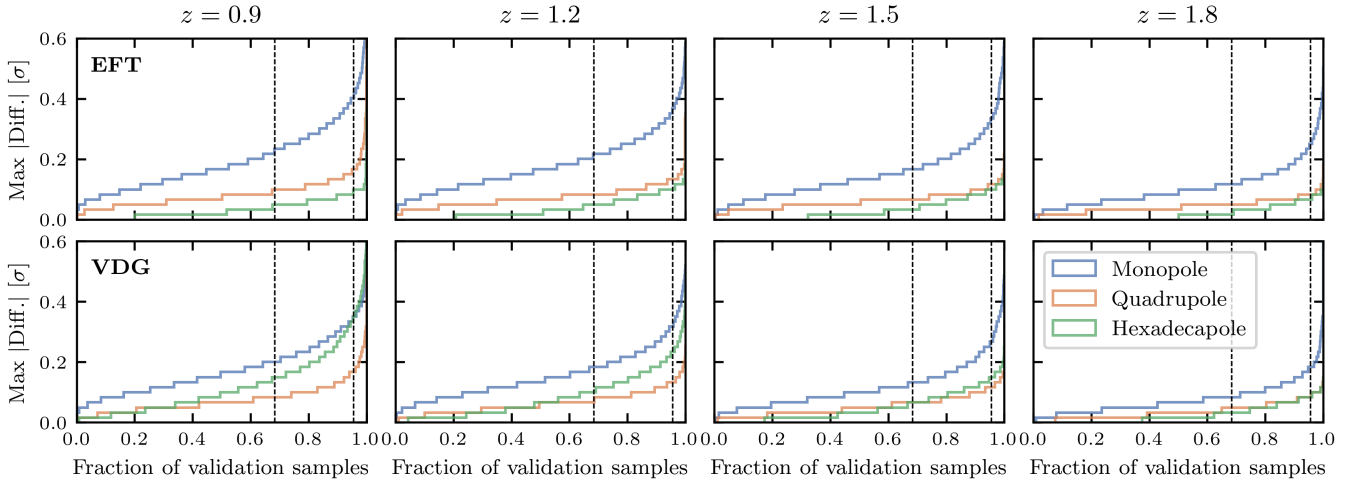


Figure C1. Cumulative histograms (over the full validation set) of the maximum absolute difference between the power spectrum multipoles computed in the exact model and with our emulator over a range of scales from $0.001 h \text{ Mpc}^{-1}$ and $0.3 h \text{ Mpc}^{-1}$. Differences are shown in units of the standard deviation of the synthetic data set described in Sec. 4.1.1. Each column corresponds to a different redshift, while the upper panels show results for the EFT model, lower panels for the VDG model. The dashed horizontal lines indicate 68 % and 95 % of the validation samples.

Table C1. Fiducial values of number densities, galaxy bias and counterterm parameters, used in the generation of the synthetic data sets described in Sec. 4.1.2.

z	$10^3 \times \bar{n} [(h^{-1} \text{ Mpc})^{-3}]$	b_1	b_2	γ_{21}	$c_0 [(h^{-1} \text{ Mpc})^2]$	$c_2 [(h^{-1} \text{ Mpc})^2]$	$c_4 [(h^{-1} \text{ Mpc})^2]$	$c_{\text{nl0}} [(h^{-1} \text{ Mpc})^4]$	N_0^P
0.9	2.043	1.370	-0.514	0.197	9.542	11.390	2.469	12.972	0.315
1.2	1.029	1.734	-0.193	0.354	15.521	17.888	4.057	78.367	0.046
1.5	0.585	2.024	0.443	0.239	11.937	18.168	3.745	33.842	-0.042
1.8	0.313	2.476	0.563	-0.112	15.377	13.322	2.958	-64.369	0.296

where $\lfloor x \rfloor$ denotes the nearest integer. Finally, we determine all unique combinations of k and μ , as well as the number of times they appear, so that we can evaluate Eq. (B1) only by averaging over those unique combinations, using their respective number of occurrences as weights. While this approximation only leads to negligible inaccuracies, it reduces the computation time and means that in the above example we can evaluate the three discretely averaged multipoles up to $k \sim 60 k_f$ without any additional computational cost compared to the standard evaluation. That means the discrete average can be straightforwardly included also in any likelihood analysis.

APPENDIX C: STATISTICS OF EMULATION INACCURACIES AT VARIOUS REDSHIFTS

For the sake of completeness, in Fig. C1 we show the cumulative histograms of the maximum absolute differences between the emulator and exact model for all four redshifts of our synthetic data sets described in Sec. 4.1.1. As in Sec. 4.2.1, the maximum differences for each multipole are obtained over a range of scales between $0.001 h \text{ Mpc}^{-1}$ and $0.3 h \text{ Mpc}^{-1}$ and overall the plot demonstrates that we get qualitatively a very similar behaviour for the validation samples at higher redshifts as for the one at $z = 0.9$ that was presented in the main text. When expressing the maximum differences in terms of the standard deviation we have adopted for our synthetic measurements, we still find the most significant discrepancies in the monopole. The fact that these decrease, however, with increasing redshift is due to the larger relative errors, $\sigma_\ell(k)/P_\ell(k)$, at higher redshifts, which are caused by our assumption of decreasing number densities and the resulting bigger contributions from shot noise to σ_ℓ .

For the EFT model we moreover see that the smallest discrepancies always occur in the hexadecapole, while, as explained in Sec. 4.2.1, they can be significantly larger in case of the VDG model. At $z = 0.9$ they exceed those of the quadrupole and with increasing redshift they become comparable. These findings are fully compatible with our results on the shifts of mean parameter values in Sec. 4.2.2, where we have seen that the spread in the shifts become smaller for the higher redshift validation samples. This is, in particular, true for the counterterm parameter c_4 , which was most affected by the inaccuracies in the hexadecapole at redshift $z = 0.9$.

APPENDIX D: PARAMETER VALUES FOR FIXED VALIDATION SET

In Table C1 we collect the values of the galaxy bias and counterterm parameters that were used to generate a set of synthetic power spectrum multipole measurements from the EFT model at four different redshifts. The tidal bias parameter γ_2 was fixed to the excursion set relation of Sheth et al. (2013); Eggemeier et al. (2020) (and thus fully determined by the value of b_1) and all other parameters not appearing in Table C1 have been fixed to zero. The number densities given here enter in the computation of the associated covariance matrices.

This paper has been typeset from a $\text{\TeX}/\text{\LaTeX}$ file prepared by the author.